










# Fully-Integrated Heterogeneous DML Transmitters for High-Performance Computing

Di Liang , Senior Member, IEEE, Member, OSA, Ashkan Roshan-Zamir , Member, IEEE, Yang-Hang Fan , Member, IEEE, Chong Zhang, Binhao Wang , Member, IEEE, Antoine Descos, Wenqing Shen, Kunzhi Yu, Member, IEEE, Cheng Li, Member, IEEE, Gaofeng Fan , Geza Kurczveil , Member, IEEE, Yingtao Hu, Zhihong Huang, Senior Member, IEEE, Marco Fiorentino , Satish Kumar , Member, IEEE, Samuel M. Palermo , Senior Member, IEEE, and Raymond G. Beausoleil, Fellow, IEEE, Fellow, OSA

(Invited Paper)

**Abstract**—Optical connectivity, which has been widely deployed in today’s datacenters and high-performance computing (HPC) systems, is a disruptive technological revolution to the IT industry in the new Millennium. In our journey to debut an Exascale supercomputer, a completely new computing concept, called memory-driven computing, was innovated recently. This new computing architecture brings challenges and opportunities for novel optical interconnect solutions. Here, we first discuss our strategy to develop appropriate optical link solutions for different data traffic scenarios in memory-driven HPCs. Then, we present detailed review on recent work to demonstrate fully photonics-electronics-integrated single- and multi-wavelength directly modulated laser (DML) transmitters on silicon for the first time. Compact heterogeneous microring lasers and laser arrays were fabricated as photonic engines to work with a customized complementary metal-oxide semiconductor (CMOS) driver circuit. Microring lasers based on conventional quantum well and new quantum dot lasing medium were compared in the experiment. Thermal shunt and MOS capacitor structures were integrated into the lasers for effective thermal management and ultra low-energy tuning. It enables a

controllable dense wavelength division multiplexing (DWDM) link architecture in an HPC environment. An equivalent microring laser circuit model was constructed to allow photonics-electronics co-simulation. Equalization functionality in the CMOS driver circuit proved to be critical to achieve up to 14 Gb/s direct modulation with 6 dB extinction ratio. Finally, the on-going and future work is discussed towards more robust, higher speed, and more energy efficient DML transmitters.

**Index Terms**—CMOS integrated circuits, diode lasers, silicon photonics, wafer bonding.

## I. INTRODUCTION

FOR decades Moore’s Law guided exponential growth of computing capacity in silicon (Si) chips, and generated data was transported globally through long-haul fiber-optic networks. They were the hardware backbone to enable today’s information era which also demands a stronger bond between electronics and photonics as data growth is nearly doubled every two years. When traditional processor-centric computing architecture and copper interconnects both reach their physical limitation and seriously limit the computation efficiency [1], new computing architectures and high-speed optical interconnects were rapidly developed to overcome performance bottlenecks.

Memory-driven computing [2]–[4] was recently proposed and rises as a revolutionary concept to lift several fundamental constrains in traditional processor-concentric architecture. This foundational concept is currently being implemented in *The Machine* [5] and *PathForward* [6] programs to debut an Exascale computer in Hewlett Packard Enterprise. High-speed, low-latency, cost- and energy-effective optical interconnects play a pivotal role here to replace traditional copper counterparts for reach from tens of meters up to two kilometers in high-performance computers (HPCs) and more and more mega-scale datacenters which offer intensive cloud-computing services [7], [8]. The mature DWDM technology typically in 50 or 100 GHz channel spacing for telecom applications promises tremendous bandwidth scalability in datacom applications as long as closely-spacing channels can be managed well in a datacom environment. Advanced liquid cooling technology maintains a typical operation temperature of 40–60 °C in HPCs, largely

Manuscript received October 17, 2019; revised November 21, 2019; accepted December 2, 2019. Date of publication December 19, 2019; date of current version July 14, 2020. (Corresponding author: Di Liang.)

D. Liang, B. Wang, A. Descos, G. Kurczveil, Y. Hu, Z. Huang, M. Fiorentino, and R. G. Beausoleil are with Hewlett Packard Labs of Hewlett Packard Enterprise, Palo Alto, CA 94304, USA (e-mail: di.liang@hpe.com; binhao.wang@hpe.com; antoine.descos@hpe.com; geza.kurczveil@hpe.com; yingtao.hu@hpe.com; zhihong.huang@hpe.com; marco.fiorentino@hpe.com; ray.beausoleil@hpe.com).

A. Roshan-Zamir was with Texas A&M University, College Station, TX 77843, USA. He is now with Texas Instruments, Santa Clara, CA 95051, USA (e-mail: ashkanroshan@gmail.com).

Y.-H. Fan and S. M. Palermo are with Texas A&M University, College Station, TX 77843, USA (e-mail: yhfanmail@tamu.edu; spalermo@tamu.edu).

C. Zhang was with Hewlett Packard Enterprise, Palo Alto, CA 94304, USA. He is now with Nexus Photonics, Santa Barbara, CA, 93105 (e-mail: chongzhang1@gmail.com).

W. Shen and S. Kumar are with Georgia Institute of Technology, Atlanta, GA 30332, USA (e-mail: w.shen@gatech.edu; satish.kumar@me.gatech.edu).

K. Yu was with Texas A&M University, College Station, TX 77843, USA. He is now with VisionICs, Nanjing, China (e-mail: kzyu@vidar.ai).

C. Li was with Hewlett Packard Enterprise, Palo Alto, CA 94304, USA. He is now with VisionICs, Nanjing, China (e-mail: cli@vidar.ai).

G. Fan was with Texas A&M University, College Station, TX 77843, USA. He is now with Microchip, Austin, TX 78730, USA (e-mail: iamfangaofeng@gmail.com).

Color versions of one or more of the figures in this article are available online at <http://ieeexplore.ieee.org>.

Digital Object Identifier 10.1109/JLT.2019.2959048

relieving many optical link design constrains. Compared with other bandwidth-scaling approaches like coherent communications [9] or ultra-high speed amplitude modulations [10], [11], DWDM approach along with on-off-key (OOK) modulation at medium data rate per channel, e.g., 10–25 Gb/s, can lead to an overall optimal solution for little latency, energy efficient photonics and driving electronics [12], and possibility to enable a high-radix switch architecture to minimize hops between computing nodes [13].

The ending decade of 2010s is an era when cloud-driven data centers and photonic links, particularly Si photonics, enable each other to scale. Integrated Si photonic platform and advanced CMOS infrastructure are ideal for such a DWDM architecture [14]. Two key technology and economic drivers, densely integrated low-loss active and passive waveguide circuit (except lasers) and excellent volume throughput and yield, become relatively trivial to accomplish. Since heterogeneous III-V compound semiconductor materials-on-Si photonic components were nicely invented and demonstrated last decade [15]–[18], rapid technical progress [19] [20] and recent commercial success [21] prove that all key photonic building blocks now can be reliably integrated on a common Si chip to excel respective material strengths and enable new structures and functionalities [22]–[24].

Here we review our recent progress on heterogeneously integrated compact light source on Si, i.e., directly modulated microring lasers and arrays, and a specially designed CMOS driver circuit [25]–[28]. High-level strategies and architecture to deploy optics in memory-driven computing systems is firstly discussed. Then two designs of microring lasers are introduced. The first one is based on traditional multiple quantum well (MQW) lasing active region plus two new integrated structures, and the other one is based on new quantum dot (QD) active region. Electrical, optical and thermal characterizations are presented in details, followed by a laser circuit model developed from static and dynamic device performance. This model provides electrical parameters for the design of customized CMOS driver with equalization functionality. Finally fabricated CMOS driver chip characterization and fully-integrated transmitter performance are presented.

## II. OPTICAL INTERCONNECT ARCHITECTURES

Fig. 1(a) shows a memory-driven HPC architecture diagram based on “memory-semantic” protocol, Gen-Z [29]. There is little or zero local memory attached to the individual computing unit (CU) including CPUs, GPUs and other system-on-chips (SOCs). Instead there is a large commonly accessible pool of memory which can physically reside in a dedicated chassis to become a memory node. Similarly there are nodes for intensive computing, I/O control or other specialized tasks. Gen-Z switches coordinate all data communication inside the node, and between nodes which is realized by photonics. Photonic interface (IF) in Gen-Z enables E/O/E conversion or future direct optical switching inside Gen-Z, and optical information transportation through low-loss optical fibers, waveguides or even free space outside Gen-Z. Dynamic data traffic in a HPC system is common. Node-to-node communications through

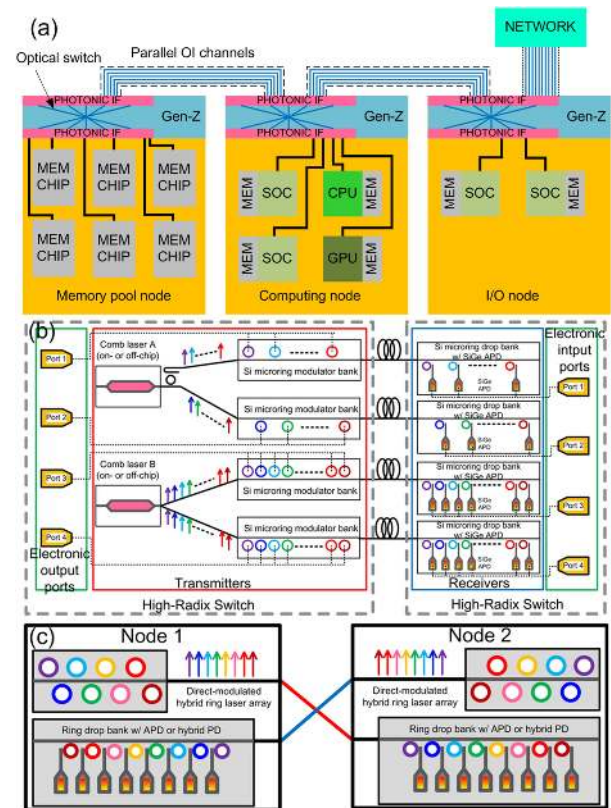


Fig. 1. (a) Schematic diagram of a memory-driven computing architecture with optical connectivity and photonic link strategies for (b) large- and (c) medium-bandwidth communication scenarios.

Gen-Z generally require tens to a few hundreds of Gb/s bandwidth, while node-to-switch port or switch port-to-switch port communications or access to external network requires Tb/s bandwidth. Such variable bandwidth demand routinely taking place in an ultimately high-radix network requires us to assemble appropriate components for different traffic scenarios.

Fig. 1(b) is a schematic of a high-channel count DWDM architecture to provide Tb/s bandwidth. Rather than bundling up several single-wavelength lasers together, a comb laser is a better choice here to generate tens of high-quality continuous-wave (cw) wavelengths with inherently fixed channel spacing [8]. This stream of multi-wavelength laser output can be split or deinterleaved to feed multiple arrays of microring resonators which provide energy-efficient data modulation and WDM function simultaneously [30]. Finally a similar array of microrings drops the signal to corresponding photodetector (PD) to finish O/E conversion. Significant reduction on the link power consumption is possible when employing highly sensitive detectors, such as CMOS-compatible SiGe avalanche photodetectors (APDs) [31], [32].

Fig. 1(c) represents a more traditional low-channel count WDM link format. 4–8 microring lasers directly modulated at 10–25 Gb/s/ch. in one array result in a good balance between aggregated transmission bandwidth and individual device control. Compactness, mirror-free structure and intrinsic WDM nature make microring or micro-disk laser array a viable choice for multi-wavelength, directly modulated, energy-efficient light source [33], [34]. Convenience to add backup lasers and to turn

TABLE I  
LINK BUDGET IN NODE-TO-NODE COMMUNICATIONS

Item	Value	
a	Bus waveguide loss	1 dB/cm
b	Single microring through port loss	0.1 dB
c	Single microring drop port loss	2 dB
d	Grating coupler loss	2 dB
e	Optical packaging loss	2 dB
f	Fiber link loss	0.4 dB/km
	Worst link budget (2 km)	12.24 dB
	Best link budget (0.1 km)	10.04 dB
g	Receiver sensitivity at 25 Gb/s	-15 dBm
	<b>Required laser output power</b>	<b>-4.96 to -2.76 dBm</b>

on/hibernated/off certain channel(s) enhances system reliability and flexibility for a sweet spot in power saving and variable data traffic operation.

Similar Si microring-based DEMUX and sensitive APDs are used in the receiver side. An projected link budget to estimate required microring laser output power in worst and best cases of 8-channel link is presented in Table I. The worst case of 12.24 dB loss means a transmitter laser signal has to bypass another 7 lasers along with the same bus waveguide and 7 microring filters in the receiver side before being dropped by the last microring to reach its APD. Vice versa for the best case. So 2.2 dB difference comes from waveguide loss and accumulated microring through port loss. -15 dBm sensitivity to achieve  $10^{-12}$  bit error rate (BER) at 25 Gb/s was used for SiGe APD-based receiver, which is a low-end estimation as APD can be more sensitive at lower data rate [32]. This estimation requires microring laser to output -4.96 to -2.76 dBm power. The rest of this paper will primarily focus on heterogeneous microring laser component and subsystem development for this link format.

### III. MICRORING LASER DESIGN

Microring and micro-disk lasers are one of the most interesting laser structures, and embrace distinct advantages and disadvantages. Its mirror-free, compact dimension and intrinsic WDM structure lead to extremely low threshold operation [35], dense integration within a small footprint [33], [36], and great potential for high-speed modulation [34]. Its traveling-wave cavity-resulted bi-stability and unidirectional lasing property is triggering for optical memory and switching applications [37]–[41]. However, challenges to achieve stable (mode hop-free, single-wavelength, unidirectional) operation, and good lasing wavelength control/correction due to fabrication imperfection and operation condition are intimidating for many commercial applications, particularly as standalone light sources. High series resistance-induced self-heating effect comes with compact dimension in general [42], [43]. So it can offset many great high-speed modulation potential as well.

Recent progress in both heterogeneous and monolithic III-V-on-Si integration provide new opportunities to these compact light sources [44]–[47]. Convenience to integrate with low-loss bus waveguide and other Si photonic integrated circuits (PICs) is a huge advantage in heterogeneous platform [33], [48], [49]. Low transparency current density and short carrier diffusion

length in QD gain medium can further drive micro-laser's threshold and dimension down. Heteroepitaxy of defect-tolerant QD gain medium on Si alleviate harsh requirement of threading dislocation density to achieve decent lasing operation and largely enhanced reliability [46], [50]. Extremely small threshold was quickly demonstrated in microring lasers on this platform [51]. With increasing progress to reduce threading dislocation density, the next major challenge is to innovate a low-loss optical coupling scheme to allow monolithic QD-on-Si PICs.

The best quality of QDs, either on native III-V substrate or Si substrate, is still obtained from molecular beam epitaxy (MBE) growth by far. While MBE is typically considered a slower and higher-cost epitaxy process than metal organic chemical vapor deposition (MOCVD), it is relatively straightforward to scale it up from a technology perspective [52]. 300 mm system is already available from vendors like Veeco and Riber with 450 mm one on the horizon waiting for the readiness of fabrication (i.e., substrate and chip manufacturing) and volume market demand. Once high-quality MBE growth of QD material on 300 mm Si substrate is ready, it is likely to gain edge on epitaxy throughput and cost over MOCVD on native III-V substrate which is 150 mm in largest size.

Two types of III-V lasing medium for O-band laser operation were selected for compact WDM transmitter development. The first one is traditional InP-based InAlGaAs multiple quantum well (MQW) structure from MOCVD growth, and the second one is GaAs-based multi-layer InAs QD structure from MBE growth.

#### A. Heterogeneous MQW Microring Laser Array

Fig. 2(a) shows the schematic cartoon of a 5-channel (ch) laser array by cascading 5 heterogeneous microring lasers along with a single bus waveguide on SOI substrate. The Si device layer and buried oxide (BOX) layer are 300 nm and 1  $\mu\text{m}$  thick, respectively. Laser epitaxial structure includes 200 nm-thick p-InGaAs contact layer, 1.5  $\mu\text{m}$ -thick p-InP cladding, InAlGaAs-based active region with 5 pairs of strained QW (1.31Q), 110 nm-thick n-InP contact layer and finally 2 pair of InP/InGaAsP superlattice (7.5 nm each). Photoluminescence (PL) measurement showed a center wavelength of 1302 nm with 39 nm full-width at half maximum (FWHM). Simulated optical confinement in MQW is 5.5%. Top-view scanning electronic microscopy (SEM) image in Fig. 2(b) exhibits a laser mesa of 50  $\mu\text{m}$ -diameter measured from the outer edge of the microring, and 3.5  $\mu\text{m}$ -wide III-V mesa width. A concentric Si microring resonator with the identical outer edge locates underneath the III-V mesa from a self-aligned fabrication process [34]. As seen from the schematic cross-sectional image in Fig. 2(c), the Si microring waveguide (1.5  $\mu\text{m}$  wide) is narrower than III-V counterpart above to suppress higher order transverse mode lasing. 1  $\mu\text{m}$ -wide bus rib waveguide was positioned 100–200 nm away from the microring resonator. About 100 nm depth was etched into the 300 nm-thick Si in the coupling region. 200 nm-thick SiO<sub>2</sub> was sputtered to passivate dry etch-exposed III-V meaus and fill up narrow coupling region. However, strong optical modal confinement in the heterogeneous microring resonator and big phase mismatch to the bus waveguide mode lead to

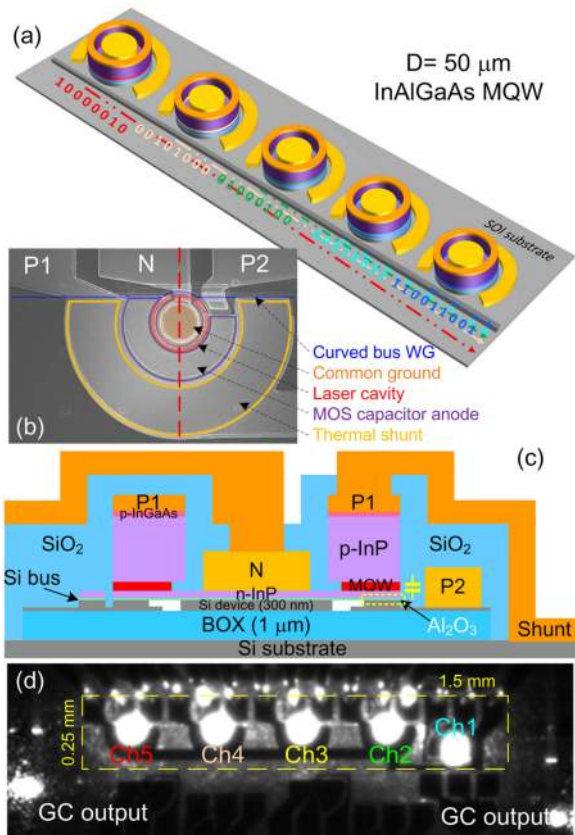


Fig. 2. Schematic of a 5-ch heterogeneous microring laser transmitter, (b) SEM image of a fabricated device, (c) cross-sectional schematic of the device with highlighted MOS capacitor, and (d) IR image of a transmitter in operation.

very minimal power outcoupling from microring to the straight bus waveguide for this  $50\ \mu\text{m}$  diameter design. A curved bus waveguide design which conformally surrounds a section of the microring resonator was used to extend the lateral evanescent coupling length and subsequently enhance the laser out-coupling strength [53]. Around 2% power outcoupling coefficient was simulated when conformal section corresponds to 11% of the microring circumference.

Two unique designs of the thermal shunt [54] and metal-oxide semiconductor (MOS) capacitor [22], [55] were both integrated in this design for the first time as illustrated in Fig. 2(c), a schematic device cross-section sliced along the red dashed line in Fig. 2(b). To overcome a thermal barrier from the thick BOX layer due to poor thermal conductivity in  $\text{SiO}_2$ , a portion of BOX outside the waveguiding region but close to the heat source (solid yellow line section in Fig. 2(b)) is selectively removed during fabrication. Then it is refilled by thermally conductive metals (Au in this work) or other materials with good thermal conductivity. Finally laser anode P1 and thermal shunt were connected by  $1.5\ \mu\text{m}$ -thick Au probe-pad to allow device Joule heat to be “shorted” to Si substrate efficiently. To form the heterogeneous MOS capacitor, 20 nm-thick  $\text{Al}_2\text{O}_3$  bonding interface dielectric is sandwiched by lightly doped ( $5 \times 10^{16}\ \text{cm}^{-3}$ ) p-Si device layer and heavily doped n-InP ( $2 \times 10^{18}\ \text{cm}^{-3}$ ) layer. Since the fundamental microring resonator mode overlaps with this capacitor, charging or discharging it by applying voltage bias to capacitor

anode P2 and common ground N introduces plasma dispersion [56], [57] and other useful electro-optic effects [23] for laser wavelength and output power tuning, and high-speed laser modulation in this new 3-terminal diode laser configuration [26].

The 5-ch. laser array is formed by slight variation in microring diameter to target a channel spacing of 0.5 nm (87 GHz in O-band). Unlike widely used 20 nm channel spacing in data-com coarse WDM (CWDM) applications, such small channel spacing was feasible and preferred in our applications here for several folds of reasons: 1) only one MQW design, i.e., single III-V epitaxial material, is required to bond on Si and provides the same maximal optical gain to each laser. Uniform operation under similar bias is also more likely. Since typical 1 dB gain bandwidth for a MQW diode laser structure is around 20 nm, such design can be easily scaled to 8 or more channels; Even more channels can fit into a single QD structure as its wider gain bandwidth [58]. However, this factor can also work against stable mode hop-free operation if there is no fine lasing wavelength selection mechanism in place as we will discuss more in section IV-B. 3) small channel spacing doesn’t require huge laser free spectral range (FSR) which is inversely proportional to laser cavity length. Reasonably long laser cavity (e.g.,  $\sim 150\ \mu\text{m}$ ) usually offers benefits like reasonable output power and thermal impedance. 3) integrated MOS capacitor provides convenient, athermal and fast wavelength control with nearly zero-power consumption [55]. Over 1 nm resonance tuning has been demonstrated with 4 V bias to the MOS capacitor [59], so 0.5-1 nm grid WDM system makes it feasible to use ultra-low power MOS capacitor-based tuning instead of power hungry thermal tuning to correct all fabrication imperfection-induced resonance overlap. Consequently, compact device structure and athermal MOS capacitor-based tuning allow close proximity between devices and small real estate for the WDM transmitter. Then global environmental temperature variation tends to result in the same impact to all lasers. When laser wavelength drifts in the same pace, cross-talk concern can be largely relieved. Since narrow band microring-based de-multiplexer (DEMUX) is used in our receiver, signals with small channel spacing can be differentiated as long as feedback loop is established to track transmitter wavelengths [60]. Aside from technical benefits above, compactness and single laser epitaxial material benefits lower chip cost.

Such a 5-ch. transmitter where all lasers were biased above the threshold is shown in an infrared (IR) image in Fig. 2(d). Two Si grating couplers (GCs) at the end of the bus waveguide were used to collect lasers’ clock-wise (CW) and counter-clock-wise (CCW) output. Excluding the GCs, the 5-ch.transmitter is  $1.5 \times 0.25\ \text{mm}^2$  in size which is limited by the  $80 \times 80\ \mu\text{m}^2$  large probe-pads for convenient wire bonding with a customized CMOS driver chip which will be discussed in details in Section VI.

### B. Heterogeneous QD Microring Laser Design

More recently we also successfully extended our heterogeneous photonic component library with QD-based comb lasers [61]–[63], microring lasers [27], [64], [65] and photodetectors

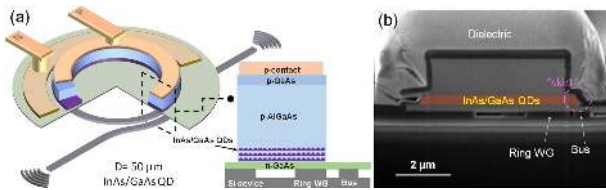


Fig. 3. (a) Side-view and cross-sectional view schematic of heterogeneous microring lasers and (b) cross-sectional SEM of a fabricated device.

[66], [67]. QD gain medium embraces multiple favorable material properties over QW counterpart, such as low transparency current density [68], excellent optical gain thermal stability [69], [70], inhomogeneous dot size-resulted wide spectral gain bandwidth [58], low relative intensity noise (RIN) [71], largely reduced sensitivity to external feedback during single-mode lasing operation [72], and large tolerance to material defects [50], [73].

The device structure of the heterogeneous microring lasers is schematically shown in Fig. 3(a) [27]. The III-V mesa consists of multiple layers of InAs/GaAs QDs with center PL wavelength around 1280 nm and FWHM of 55 nm. p- and n-doped GaAs/AlGaAs layers sandwiches the 8-layer QD stack to confine the optical mode as well as to offer electrode contacts. Similarly, 50  $\mu\text{m}$  in diameter microring lasers with 5  $\mu\text{m}$ -wide III-V mesa were built on a 400 nm-thick Si device layer and 1  $\mu\text{m}$ -thick BOX layer in this first development run. Unlike our routinely used self-aligned fabrication process [34], the 1.5  $\mu\text{m}$ -wide Si microring and 550 nm-wide bus waveguides was formed on the SOI substrate prior to wafer bond the QD epitaxial material this time. 248 nm DUV project photolithography with <50 nm overlay accuracy was used to pattern the Si microring and bus waveguide, and then define concentric III-V microring mesa up III-V epitaxial transfer. Thus mesa dry etch step didn't have to etch through the entire III-V stack, but stopped above the n-GaAs contact layer. This allowed laser cathode to be placed outside the microring mesa, similar to heterogeneous micro-disk lasers [74]. The same sputtering procedure was used to encapsulate the III-V mesa with 800 nm  $\text{SiO}_2$ . Detailed fabrication flow can be found in [27]. Fig. 3(b) shows the cross-sectional SEM image of the device. Due to conservative and imperfect mesa dry etch, a "skirt" was resulted. It results in noticeable enhancement of the optical coupling confirmed by both simulation and experimental results, but also introduces some optical loss. Similar curved conformal bus waveguide was used here as well to enable power outcoupling coefficient as large as 20% [27]. Two Si GCs at the end of the bus waveguide are used to collect output power. Only individual devices, no laser array, were designed and fabricated with QD laser active region in this work.

#### IV. HETEROGENEOUS LASER PERFORMANCE

All laser characterization was conducted by placing the device under test (DUT) on a copper stage with thermoelectric cooling (TEC) control and in a cw mode.

##### A. Light-Current-Voltage (LIV) Characteristic

Fig. 4(a) shows a typical room-temperature (RT) LIV of the 5-ch. MQW microring laser array when only a single-side output

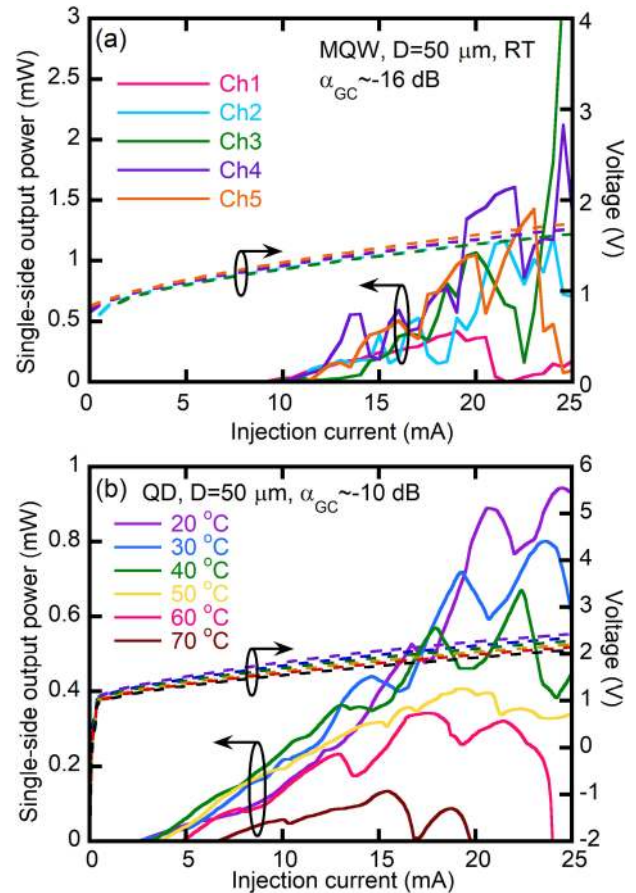


Fig. 4. LIV characteristic of (a) MQW laser array at room temperature and (b) single QD laser from 20 to 70  $^{\circ}\text{C}$  stage temperature.

power was collected. Almost identical IV curves indicate similar series resistance in the range of 24–27  $\Omega$  between 10–25 mA injection current and similar joule heating at the same bias points, which favors to obtain uniform channel spacing. Small variation in threshold of 9–12 mA were measured as well, leading to 1912–2550  $\text{A}/\text{cm}^2$  threshold current density. But extremely messy LI curves indicate frequent mode hops and lasing direction switches due to a combined effect of strong reflection from the Si GCs and small FSR vs. MQW gain bandwidth. It is noted that GC has a large  $\sim 10$  dB coupling loss at designed 1310 nm because of undesirable 1  $\mu\text{m}$ -thick BOX, minimal lithography feature size of 200 nm, and imperfect fabrication for unexpected  $\sim 40$  nm red shift of primary lasing wavelength to 1340–1350 nm from this batch of epitaxial material. Reflection rises to more than 18% in this wavelength range and triggers complex coupled cavity effect and potential self-injection locking or other instability when bias current increases. Injection locking from one laser to another was not observed as long as their wavelengths were separate. Depending on the curved section length in bus waveguide, i.e., effective mirror loss, statics from individual devices on the same chip show laser threshold of 5 to 14 mA and up to 8% single-side wall-plug efficiency at RT. Temperature-dependent LIV characterization was not able to conduct in time unfortunately before packaging onto the PCB board with CMOS driver chip. However, up to 105  $^{\circ}\text{C}$  cw lasing

was achieved on devices with the same MQW epitaxial material, fabrication process and largely identical thermal shunt design. Characteristic temperature  $T_0$  was extracted to be 126 K in 20–60 °C and 61 K in 60–105 °C. Both  $T_0$  values were believed to be underestimated since they were from threshold numbers in cw instead of pulsed mode. Thermal impedance is 364 °C/W. Much higher value of 11500 °C/W was reported on much smaller size heterogeneous micro-disk lasers ( $D = 6 \mu\text{m}$ ) without special thermal management design. More details can be found in Ref. [54], [42].

Typical temperature-dependent LIV curves of the QD device counterparts are plotted in Fig. 4(b). cw lasing was maintained up to 70 °C. When stage temperature rose from 20 to 70 °C, threshold current increased from 2.5 to 7 mA, corresponding to 340–952 mA/cm<sup>2</sup> threshold current density, and series resistance decreased from 44 to 37  $\Omega$ . This represents nearly 6 $\times$  reduction in the threshold current density when switching from InAlGaAs MQW to InAs/GaAs QD active region in our heterogeneous platform. Majority of over one hundred measured devices lased between 1.5 to 4 mA, including several sub-mA threshold as low as 0.7 mA at 20 °C, corresponding to a record-low 90 mA/cm<sup>2</sup> threshold current density for all micro-cavity lasers on Si to our best knowledge. However, device with sub-mA threshold outputted power below 1  $\mu\text{W}$  due to minimal outcoupling coefficient. With 10 dB measured GC loss included, 0.9 mW single-side output power was measured at 20 °C in Fig. 4(b), and majority of devices delivered 0.07 to 1 mW output power depending on variable coupling coefficient in design. This is about 3 $\times$  lower than the average maximum power we measured from heterogeneous QW counterparts at the same injection current. Due to intrinsic lower optical gain in QD material, only  $\sim$ 2% maximal single-side WPE was measured at 20 °C. Further improvement to enhance optical confinement in active region and outcoupling coefficient, reduce dimension slightly, and reduce cavity loss and series resistance as much as possible could further reduce the threshold and boost the WPE [75] to reach the required laser output power in Table I in 40–60 °C operation environment. Alternatively, a heterogeneous QD semiconductor optical amplifier can be readily integrated after an array of microring lasers or as a preamplifier in the receiver end to boost up multi- $\lambda$  signal. Low leakage was measured in both MQW and QD lasers, qualitatively indicating good passivation to the dry etch-exposed active region. Less than 20 nA of dark current at  $-1$  V reverse bias was typical for MQW lasers, but only tens of pA was observed in QD lasers at the same reverse bias. The translated dark current density is different by three orders of magnitude, showing that QD gain medium is indeed much less subject to surface states and non-radiative recombination than QW counterparts as expected. QD material is also known for enhanced high-temperature operation, and we have demonstrated over 100 °C operation in our comb lasers [63]. For a few devices with low series resistance, e.g., 16  $\Omega$ , the output power didn't show thermal rollover until 35 mA current injection (14 $\times$  threshold), indicating much better temperature stability in QD gain region. However, thermal impact becomes apparent in devices suffering from higher series resistance-induced excessive joule heating. The n-type specific contact

resistances on n-GaAs was measured to be  $1 \times 10^{-4} \Omega/\text{cm}^2$ , two orders of magnitude higher than our typical results on previous InP counterparts. The large contact resistance is likely due to the low contact anneal temperature at 300 °C. While higher anneal temperatures should result in better contacts, the large thermal mismatch between GaAs and Si could generate defects or weaken bonding strength at those temperatures. Additional process optimization is required, and thermal shunt will also be implemented to further minimize thermal impact. Underestimated characteristic temperature  $T_0$  from cw threshold current in Fig. 4(b) is 128 K in 20–40 °C and 37 K in 40–70 °C, which are comparable to monolithic QD microring lasers on silicon [51] and 5 mm-long QD Fabry-Perot lasers on native III-V substrate [76]. Infinite or even negative  $T_0$  in QD lasers have been reported [77], [78], as well as relatively low  $T_0$  numbers in 20–60 K [79], [80], indicating that multiple factors like p-type doping, inhomogeneous banding and dislocation density all contribute to temperature performance. More thermal management discussion will be provided in Section IV-C below.

The ripples on the LIs curve represent both modes competition among longitude modes and the direction switch between CW and CCW directions. Wide gain spectral bandwidth in QD material indeed encourages more frequent mode hops. More details will be discussed in Section IV-B below. Unidirectional lasing designs [81] will integrate in the next design to stabilize lasing direction. Designs to use coupled cavity and fine wavelength selection component [82] will also be studied to enable mode hop-free operation.

### B. Spectral Measurement

Spectral characterization for both MQW and QD microring lasers was carried out at RT. Fig. 5(a) shows high-resolution spectrum of a single heterogeneous MQW microring laser at 27 mA current injection. An expected FSR around 3.3 nm with an excellent extinction ratio over 65 dB for primary lasing mode was measured. Good side-mode suppression ratio (SMSR) of 35 dB were achievable at certain injection levels (27 mA in this case), but multiple mode lasing was typical due to small FSR. This is illustrated by the wavelength contour vs. injection current in Fig. 5(b). Much more consistent single-mode lasing from MQW active region designs has been observed in 30  $\mu\text{m}$  or smaller diameter devices with larger FSR previously.

Figs. 5(c) and (e) are respective spectra (medium resolution) for 4- and 5-ch. arrays both with 0.5 nm channel spacing design but 5-ch. one was finely tuned by biasing the integrated MOS capacitors. In Fig. 5(c), lasers of channel 1 to 4, respectively biased at 17.2, 17.2, 17.0 and 16.2 mA, show consistent 0.46 nm channel spacing,  $\geq$ 50 dB extinction ratio (limited by the instrument noise floor) with  $<$ 5 dB peak power variation, and  $>$ 20 dB SMSR. It is only 0.04 nm smaller than 0.5 nm designed channel spacing, indicating achievable good control to small dense WDM-type of channel spacing. In addition, a 0.1 nm wavelength blue shift was observed in a single device when 5 V bias was applied between terminals P2 and N in Fig. 5(d). Leakage current through the capacitor was below the current source limit of 10 pA. Previous work showed fA-level leakage current within 6 V bias [55].

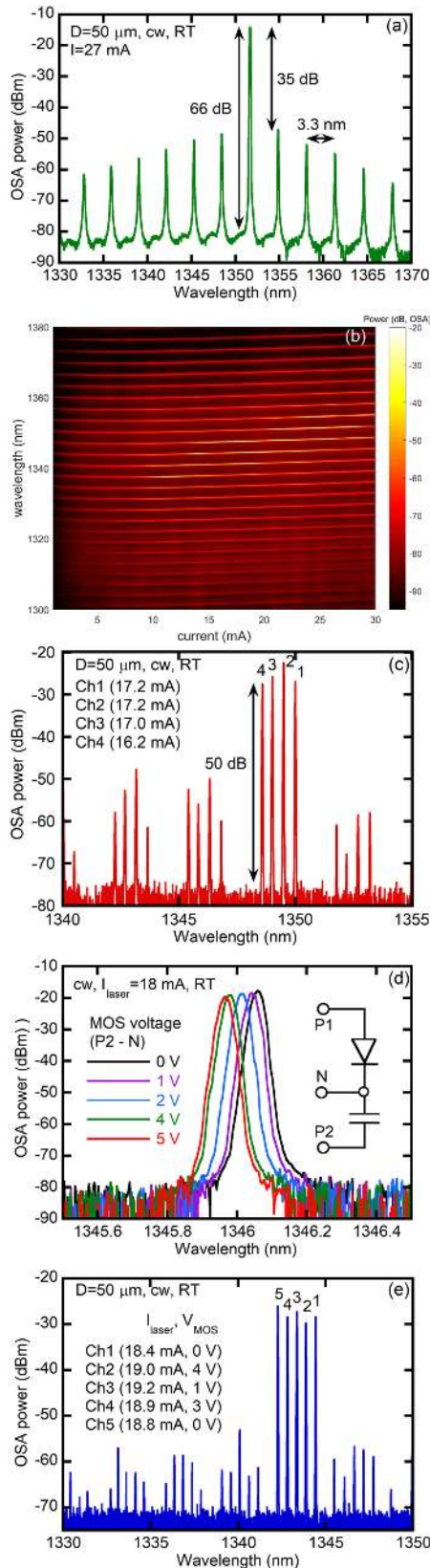


Fig. 5. (a) Measured spectrum of a heterogeneous MQW microring laser at 27 mA injection current, (b) contour map of lasing wavelength as a function of injection current for the same devices, (c) spectrum of a 4-ch. array without fine tuning through integrated MOS capacitor, (d) single laser spectrum at current injection current and variable bias on MOS capacitor, and (e) spectrum of a 5-ch. array with fine tuning through integrated MOS capacitors.

This extra freedom of phase control enabled us to fine tune a 5-ch. array to exhibit a consistent 0.5 nm channel spacing and  $>30 \text{ dB}$  SMSR in Fig. 5(e). It is noted that in the receiver side we design DEMUX using array of Si microring resonators whose FSR is over 15 nm and not equal to  $n \cdot \text{FSR}_{\text{laser}} + m \cdot \Delta\lambda$  where  $n$  and  $m$  are integers ( $n > 0$ ,  $m \geq 0$ ) and  $\Delta\lambda$  is the channel spacing. It can prevent DEMUX microring from accidentally dropping any side modes from the same laser or neighboring ones to the same receiver channel, so over 40 dB SMSR for conventional single-mode operation is not strictly required to achieve crosstalk-free data transmission.

Fig. 6 are spectra from the single QD microring lasers under different injection current. Due to larger and relatively flat optical gain envelop in QD gain region and even smaller FSR of 3 nm from larger group index in GaAs-based materials, multiple spectral mode lasing with  $<10 \text{ dB}$  SMSR is common in many injection levels (Fig. 6(a)). Compared with MQW lasers, QD ones could easily have more than three strong lasing spectral modes at a fixed current injection, and they are not necessarily in consecutive mode numbers. For example, mode at 1302.27 nm is a weak lasing mode adjacent to strong ones when the device received 8 mA current injection in Fig. 6(a). This phenomenon is more obvious in the contour wavelength map in Fig. 6(b). This is a signature of inhomogeneous broadening effect in QD active region [83]. But it was interesting to still observe relatively stable single-mode lasing as shown in Fig. 6(c). SMSR over 31 dB and up to 45 dB was achieved within a smaller injection current range from 23 to 31 mA. We believe that there are likely some local QD regions with small dot size variation, leading to strong gain with narrow spectral bandwidth. When microring laser mesa happens to largely overlap with such a localized QD region, and a laser resonance mode matches to the local gain peak, good SMSR lasing can occur. Temperature-dependent spectral measurement show wavelength drift at  $0.08 \text{ nm}/^\circ\text{C}$ , similar to what we and others observed in InP-based MQW counterparts [42].

### C. Thermal Management

Micro- and nano-lasers are well known to suffer from joule heating easily because of smaller dimension and intrinsically high thermal impedance. Thick BOX layer in SOI substrate makes it worse to act as a thermal barrier to prevent efficient heat dissipation to the Si substrate [43], [84], [85]. As discussed in Section III-A, a thermal shunt design was implemented in the MQW microring laser structure shown in Fig. 2(c). 30–40% reduction on thermal impedance has been reported in our earlier work to enable up to  $105 \text{ }^\circ\text{C}$  cw lasing in the same InP-based MQW active region design [54]. Thermal reflectance measurement was conducted to study the effectiveness of the thermal shunt in this batch of MQW lasers. Two configurations of thermal shunt and corresponding probe-pad layout, A and B, were designed as illustrated by the mask snapshots in Fig. 7(a). Design A was for DC-only bias control to the MOS capacitor section in orange and direct modulation was achieved by high-speed modulating the current signal to the diode laser active region. Design B was to apply the high-speed voltage signal to the MOS capacitor region to modulate the laser phase and intensity while keeping laser bias constant. To match with

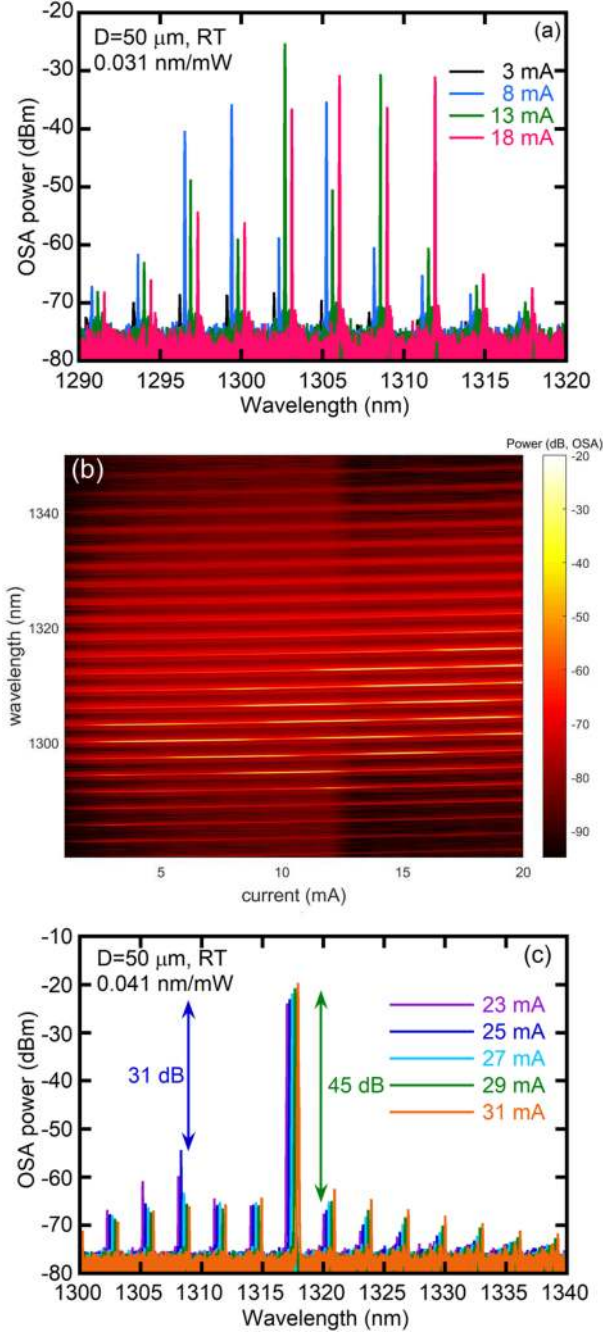


Fig. 6. (a) Measured spectra of a heterogeneous QD microring laser at 3, 8, 13, and 18 mA current injection, (b) contour map of lasing wavelength as a function of injection current, and (c) spectra of another QD microring laser at 23–31 mA current injection.

bond pad layout in the CMOS driver, Design B has a P1-P2-N probe-pad configuration from left to right hand side, instead of P2-N-P1 in Design A. Since laser anode P1 connects with the thermal shunt in green to extract heat from the top of the III-V mesa, overlap between P2 and P1 in Design B was avoided to minimize parasitic capacitance and noise from Si substrate. Therefore, thermal shunt region was divided into two sections in Design B to make room for probe-pad to reach MOS capacitor anode region. This change slightly reduces the heat extraction efficiency to the thermal shunt for Design B because of smaller

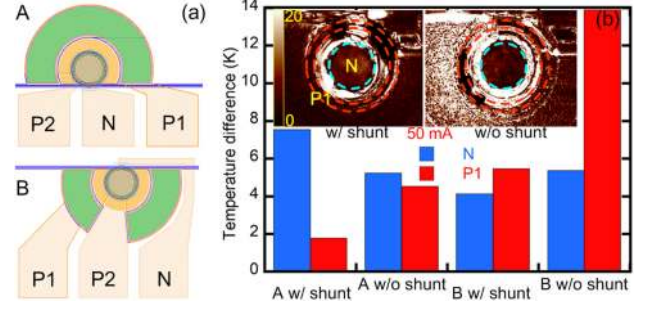


Fig. 7. (a) Snapshots of mask designs of A and B and (b) measured surface temperature comparison for devices with and without thermal shunt at 50 mA injection; inset: thermal reflectance images.

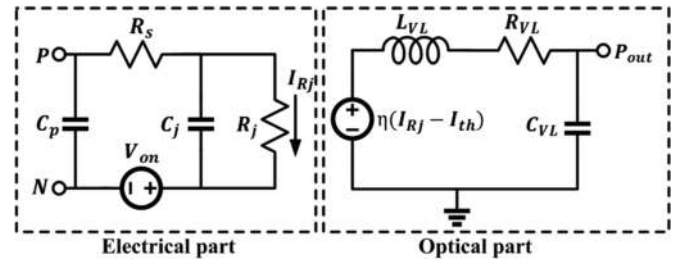


Fig. 8. Equivalent circuit model of microring lasers.

thermal shunt area. Multiple monitoring points on the terminals N and P1 are highlighted in inset images of Fig. 7(b). Devices were tested on a stage with fixed temperature of 20 °C while measured temperature values in Fig. 7(b) were increased portion above stage temperature. Average increased surface temperature values due to joule heating under 50 mA current injection show over 60% reduction in P1 which directly indicates the junction temperature for both types of probe-pad configurations. This measurement validated good effectiveness of the thermal shunt design when co-integrating with the 3-terminal laser structure. Both designs will be implemented in QD version of devices soon. We note here that high-speed modulation to the MOS capacitor region (Design B) showed great potential for much higher modulation bandwidth [26]. This topic will be discussed in details in a future publication.

## V. MICRORING LASER CIRCUIT MODEL

In order to provide good reference for CMOS driver design, a microring laser model that includes both electrical equivalent circuit and optical dynamics components was developed. As illustrated in Fig. 8, the model's electrical part describes the laser junction, represented by junction capacitance  $C_j$  and resistance  $R_j$ , an equivalent series resistance  $R_s$ , and the parasitic capacitance  $C_p$  between anode and cathode terminals of the diode laser. Optical dynamics are captured with a junction current dependent RLC equivalent circuit ( $R_{VL}$ ,  $L_{VL}$ , and  $C_{VL}$ ) that is driven by a current-controlled-voltage-source  $\eta(I_{R_j} - I_{th})$  where  $\eta$ ,  $I_{R_j}$ , and  $I_{th}$  are device slope efficiency, injection current and threshold current, respectively. The  $L_{VL}$  and  $R_{VL}$  are defined



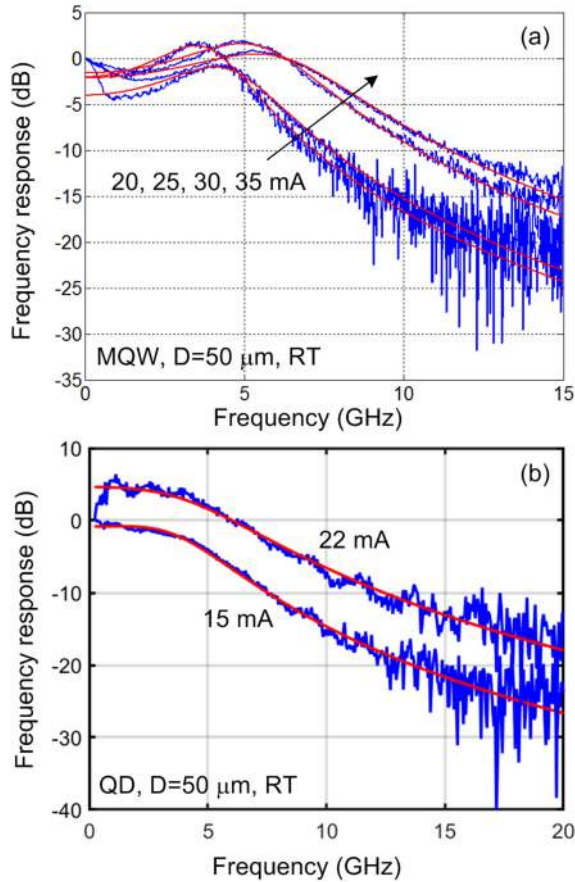


Fig. 9. Measured  $S_{21}$  response and curve fitting results at different injection currents for (a) MQW and (b) QD microring lasers.

by Eqs. (1) and (2) [28], [86].

$$L_{VL} = 1 / \{4\pi^2 C_{VL} D^2 (I_{Rj} - I_{th})\} \quad (1)$$

$$R_{VL} = (K f_r^2 + \gamma_0) L_{VL} \quad (2)$$

where  $D$ ,  $K$ ,  $f_r$  and  $\gamma_0$  respectively represent directly modulated laser dynamic parameters D-factor, K-factor, resonance frequency, and damping factor offset. Measured  $S_{11}$  curves for both MQW and QD lasers were utilized to determine the electrical parameters by curve fitting the low-pass RC electrical model. The optical parameters for these two types of devices were then extracted by curve fitting measured  $S_{21}$  curves at different injection current levels, as shown in Fig. 9. Both types of devices show similar 3 dB bandwidth around 8 GHz. Small outcoupling coefficient resulted low output power limits bandwidth in MQW lasers primarily. Current device dimension of 50  $\mu\text{m}$  doesn't favor large bandwidth as well. InAs/GaAs QD lasers typically show direct modulation bandwidths around 10 GHz or less due to strong gain compression and low saturated gain [87], [88]. Table II summarizes the total extracted parameters. The MQW laser parameters were in development of the first test vehicle for this full electronics-photonics integrated transmitter demonstration, as the CMOS transmitter IC was developed prior to the heterogeneous QD microring lasers.

TABLE II  
EXTRACTED PARAMETERS OF MQW AND QD MICRORING LASERS

Parameters	Value	
	MQW	QD
Junction Capacitance ( $C_j$ ) [ fF ]	590	1200
Junction Resistance ( $R_j$ ) [ $\Omega$ ]	20.3	20.27
Series Resistance ( $R_s$ ) [ $\Omega$ ]	18.2	27.38
Parasitic Capacitance ( $C_p$ ) [ fF ]	20	217
Turn-on Voltage ( $V_{on}$ ) [ V ]	1.0	1.2
D-factor ( $D$ ) [ GHz/mA <sup>0.5</sup> ]	1.15	1.09
K-factor ( $K$ ) [ ns ]	0.55	1.53
Damping Factor Offset ( $\gamma_0$ ) [ ns <sup>-1</sup> ]	0.16	7.24

## VI. CMOS DRIVER DESIGN AND CHARACTERIZATION

Fig. 10(a) shows the block diagram of the half-rate five channel integrated CMOS driver [25]. The on-chip pseudorandom binary sequence (PRBS) generator outputs 8 bits of parallel data which is then serialized to quarter-rate. A quarter-rate delay generator creates 1-UI delayed versions of data as well as the main data. The quarter-rate bits are then serialized to full-rate by the following two stages of 2:1 serializers. The rise/fall signals are generated in the pre-driver and are combined with the main data at the output current-mode logic (CML) driver to drive the microring laser devices. An off-chip half-rate clock is received and amplified by a global CML buffer and distributed to channels using an on-chip transmission line. After being received and amplified by a local CML buffer the clock amplitude is converted to rail-to-rail swing by a CML to CMOS converter. CMOS buffers with adjustable pull-up/down are used to correct the clock duty-cycle. The CMOS buffers drive the final 2:1 MUX as well as clock dividers to generate lower rate clocks for driving 4:2 and 8:4 serializers and PRBS generator. A detailed block diagram of the data-path and pre-driver after 8:4 serializer is shown in Fig. 10(b). Two 1-UI delayed versions of data are generated with independent control over polarity which is then serialized to full-rate. The pre-driver generates positive or negative pulses on fall/rise outputs depending on fall/rise\_sign control bits during the falling/rising transitions of the data. The CML output driver of Fig. 10(c) consists of three parallel differential pairs combining the fall/rise signal with the data implementing the 2-tap asymmetric FFE function. Three 4-bit current DACs are used in the source of differential pairs to independently control rising and falling FFE tap weights and current swing, providing a 40 mA maximum current swing as well as 10 mA (each) maximum additional currents activated during falling and rising edges to increase or decrease the current during these transitions. A 4-bit current digital-analog converters (DACs) is used to provide up to 20 mA of bias (minimum current to control laser bandwidth. The replica-load is biased with an additional current DAC. Laser wavelength tuning is

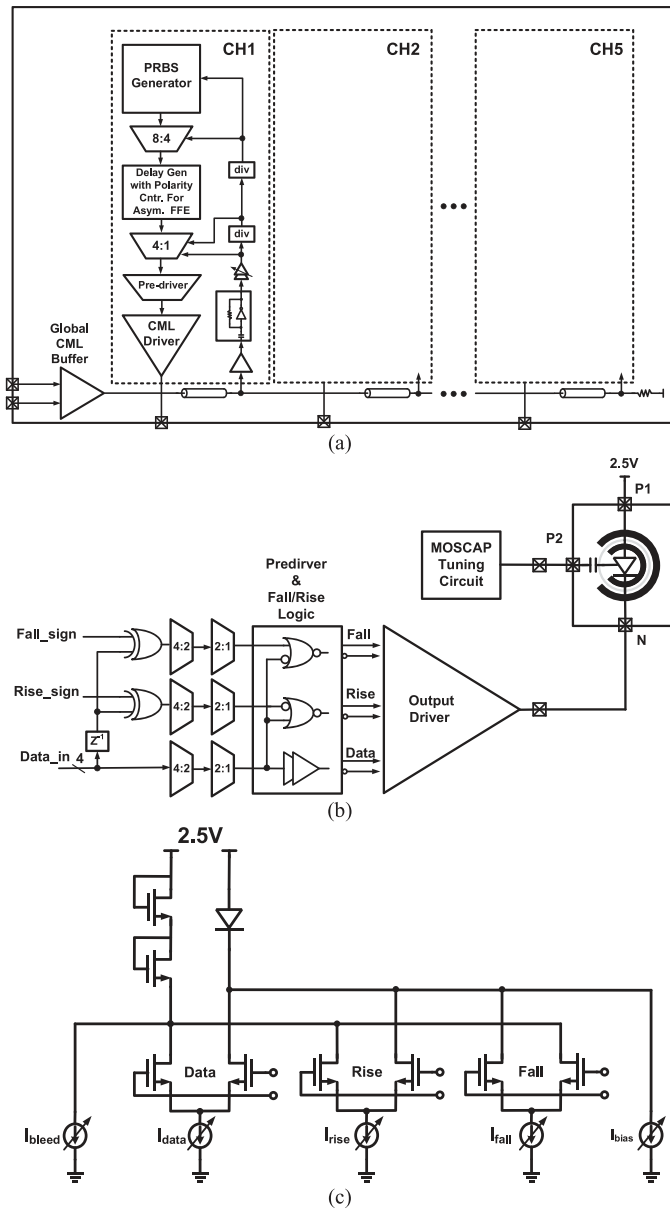


Fig. 10. (a) Block diagram of the proposed 5 channel driver, (b) CMOS driver data-path and connection to microring device, and (c) schematic of CML output driver with asymmetric FFE.

achieved by engaging a high voltage (3.6 V) DAC controlling the DC voltage of MOS capacitor terminal (P2).

Optical measurement results of Fig. 11(a) for a clock pattern data shows how the non-linear current dependent bandwidth of device results in slow overdamped falling edge and fast underdamped rising edge with ringing. The same behavior was predicted by simulated 10 Gb/s pulse response of our microring laser model (Fig. 11(b)). The proposed asymmetric FFE with independent control over fall/rise settings and the sign can efficiently compensate for this non-linear laser behavior.

The CMOS driver functionality is tested by connecting the driver to a high bandwidth sampling scope through printed circuit board (PCB) trace, SMA connectors, and cables with the required DC bias voltage supplied to the driver through a

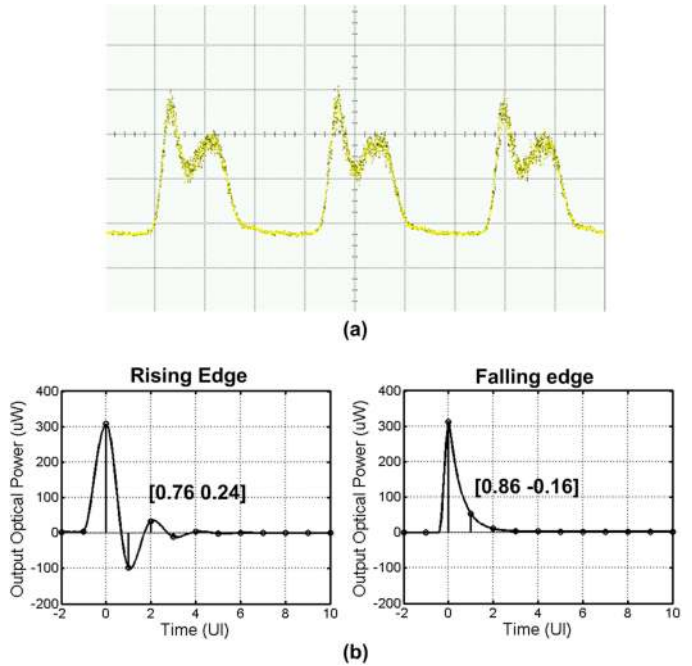


Fig. 11. (a) Measured microring response to a clock pattern and (b) simulated rising and falling pulse response of the microring device.

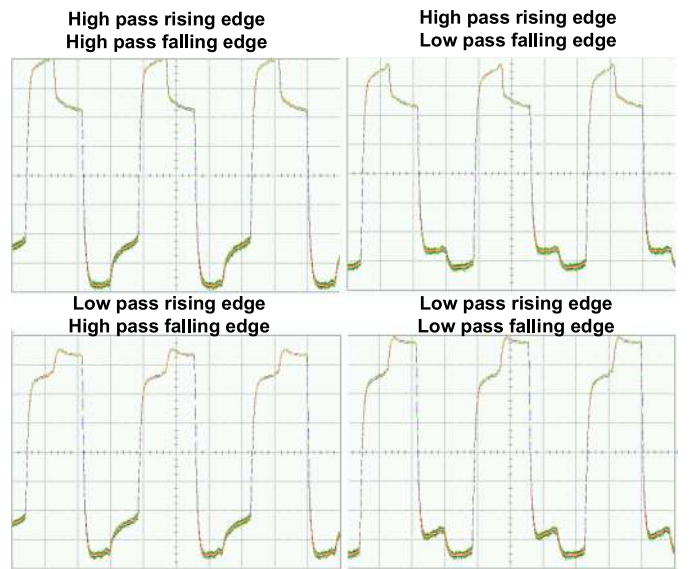


Fig. 12. Measure FFE response to 1100 pattern with different high-pass/low-pass setting for rise/fall edges.

bias-tee. In order to check the functionality of the asymmetric feed-forward equalization (FFE) equalizer, a fixed 1100 pattern is transmitted while using different equalizer signs for rising and falling edges. As illustrated in measured results in Fig. 12, the driver successfully implements all four combinations of high-pass/low-pass for falling/rising transitions. Figs. 14(a) and (b) show the measured 16 Gb/s eye-diagram of the driver with and without FFE equalizer. As shown in Fig. 13(a), the PCB trace and cable loss causes significant jitter and eye-height reduction resulting in 32 ps eye-width and 90 mV<sub>pp</sub> of eye-height. The

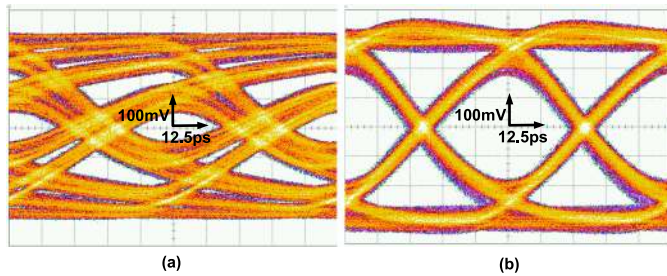


Fig. 13. Measured CMOS driver 16 Gb/s eye-diagrams (a) without FFE and (b) with FFE.

channel loss can be efficiently compensated when engaging the FFE equalizer (high pass for both edges) as illustrated in Fig. 13(b) providing 50 ps of eye-width and 350 mV<sub>pp</sub> of eye-height.

## VII. INTEGRATED TRANSMITTER CHARACTERIZATION

The CMOS driver is fabricated in a 65 nm CMOS process with all high-speed blocks, expecting the output driver and wavelength tuning DAC working with a 1.2 V supply. The low-speed MOS capacitor tuning DAC uses a 3.6 V supply to provide sufficient wavelength tuning range, utilizing high-voltage I/O transistors.

### A. Integrated WDM MQW Transmitter

A hybrid integration of photonic chip and CMOS driver is done by direct wire-bonding of closely placed photonic and CMOS dies as shown in Fig. 14(a). The CMOS driver is directly bonded to the board to provide, supply voltages, control signals and half-rate clock. Fig. 14(b) shows the high-speed measurements test setup. A high-speed pattern generator is used as a clock source to provide the half-rate clock to the driver chip as well as a trigger signal for the high-speed sampling scope. The CMOS driver supplies the photonic chip with a 2.5 V supply as well as the high-speed data. The modulated light is coupled out of the chip, and the eye diagrams has been measured by the sampling scope with the optical module. Fig. 15(a) shows the 12 Gb/s measured eye-diagram with no FFE equalization. As shown here, the large ringing on the rising edge and slow falling edge have significant negative effect to the quality of the eye diagram. Fig. 15(b) shows how the 2-tap asymmetric FFE can reduce the rising edge ringing while enhancing the falling edge speed improving both vertical and horizontal eye openings. The hybrid integration of microring laser and the CMOS driver with FFE equalization allows for data-rate increase from previously maximum measured 10.5 Gb/s using benchtop equipment (Fig. 15(c)) to 14 Gb/s as illustrated in Fig. 15(d). The demonstrated optical transmitter achieves 5.7 dB of extinction ratio at 14 Gb/s, and consumes 144.5 mW of power in total, equivalent to an energy efficiency of 10.3 pJ/bit.

### B. Integrated QD Transmitter

The same hybrid integration approach was utilized to integrate a single QD microring laser with an individual channel of the

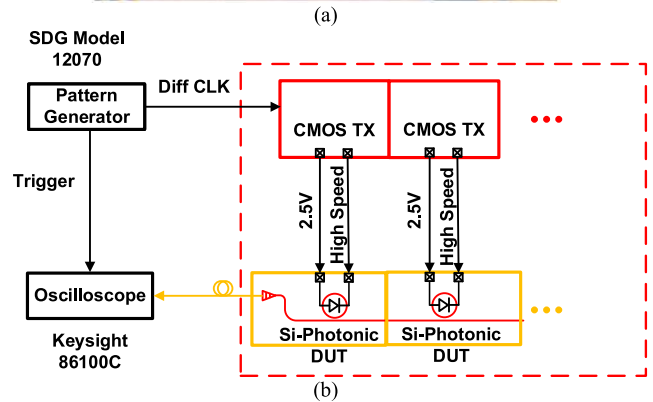
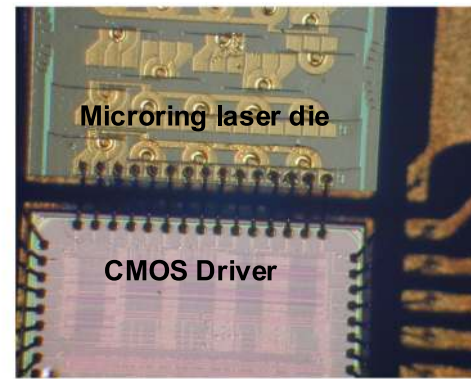


Fig. 14. (a) Hybrid-integrated microring laser transmitter prototype and (b) high-speed measurements test-setup schematic.

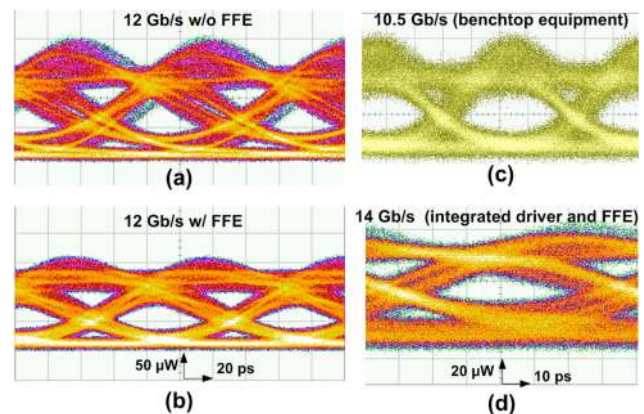


Fig. 15. Measured 12 Gb/s optical transmitter eye-diagrams (a) without FFE, (b) with FFE, and measured eye-diagrams using (c) bench-top equipment at 10.5 Gb/s and using CMOS driver with asymmetric FFE at 14 G/s.

same 5-ch. CMOS driver chip. Based on the developed QD microring laser co-simulation model, Figs. 16 show the simulated 12 Gb/s optical eye diagram before and after applying the FFE equalizer, respectively. Activating the asymmetric 2-tap FFE allows for opening of a previously closed eye and significant performance improvement. Similar performance improvement was observed in the measured eye diagrams at 12 Gb/s in Figs. 16(c, d). A little bit noisy eye diagram is likely from potential crosstalk from some visible imperfection in wire bonding and mismatch in laser parameters between QD and MQW lasers as this driver circuit was designed specifically for MQW

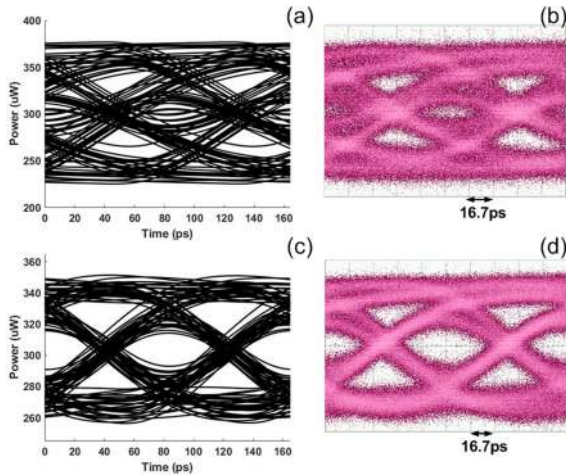


Fig. 16. (a), (c) Simulated and (b), (d) measured optical eye diagrams of QD microring lasers driven by the CMOS driver chip at 12 Gb/s before applying asymmetric FFE (a), (b) and after applying asymmetric FFE (c), (d).

laser structure. Over 4 km error-free transmission experiment at 12.5 Gb/s was successful when high-speed signal was generated by bench-top equipment, and up to 15 Gb/s open eye diagram was measured, translating to an energy efficiency of 1.2 pJ/bit [27]. To our best knowledge 15 Gb/s in OOK format is the fastest direct modulation rate for O-band QD lasers on Si [89], [90]. A revised CMOS driver design based on more advanced technology node is promising to bring the total QD DML transmitter energy efficiency to  $<2.5$  pJ/bit.

### VIII. CONCLUSION AND FUTURE WORK

To summarize, we reviewed our most recent work in two types of heterogeneous microring lasers on Si, and first attempt to develop a CMOS driver circuit to directly modulate the microring lasers and WDM laser arrays. Advantages and imperfections in design and fabrication plus intrinsic material properties were openly discussed in details here. Traditional InP-based MQW active region provides more optical gain, subsequently more laser output power while InAs/GaAs QD active region instantly reduces the threshold and power consumption by a factor of 6. Effective thermal shunt and MOS capacitor structures are integrated into the MQW laser fabrication process successfully for the first time. Uniformly spaced 5-ch. laser array with 0.5 nm channel spacing is demonstrated by using MOS capacitor tuning as an independent control freedom. Single-mode operation is possible in both optical gain materials but undesired multiple mode lasing is common. Based on measured laser performance, a laser circuit model is developed to provide reference parameters for customized CMOS driver design in a 65 nm node. Fabricated CMOS driver chip with equalization functionality minimizes nonlinear effect in directly modulated lasers, and finally results in fully-integrated transmitters capable of up to 14 Gb/s/ $\lambda$  (aggregated 70 Gb/s/transmitter) clean operation with nearly 6 dB extinction ratio and 10.3 pJ/bit energy efficiency.

Several impressive DML-based single-wavelength and CWDM-4 edge-emitting transmitters [91]–[93] clearly showed

advantages of simplicity, compactness and energy efficiency over externally modulated counterparts for  $\leq 2$  km transmission. Our on-going research priority is to further develop heterogeneous QD microring lasers to eventually build both microring and comb laser on the same chip in a Gen-Z switch to provide dynamic bandwidth and good energy efficiency for data transmission in memory-driven computing HPCs. Improvement on laser efficiency will involve developing a better etch process for smoother III-V and Si etch profile, enhancing outcoupling strength, and optimizing laser epitaxial and cavity structure [91]. More stable single-wavelength and unidirectional operation can be achieved by several designs: a) integrate grating-based wavelength selection mechanism [82] and an unidirectional laser design [81], [94]–[98] into the laser cavity; b) selectively break parity-time (PT) symmetry in microring laser cavity [99]; c) execute optical injection locking (OIL) [38]. Our recent experiment confirmed that OIL enabled 45 dB or more SMSR to over ten resonance modes in the same heterogeneous QD microring lasers within material gain envelope when tuning the master laser wavelength to one of the slave microring laser resonances [100]. A new concept of integrating the comb laser as a multi-wavelength master laser to lock multiple microring slave lasers was proposed with proof-of-concept experimental support. It could be an attractive solution to resolve lasing direction switching and mode hop issues simultaneously. To use only one additional master laser for many microring slave lasers minimizes the energy and solution cost of such an OIL system, and our heterogeneous integration platform is ideal to build this system on the same chip. Improved metallization in QD lasers is necessary to minimize joule heating effect and improve energy efficiency, and integrated thermal shunt structure will add another layer of positive thermal management to make it more robust. QD intrinsic material property-determined poor direct modulation bandwidth is hard to overcome, but higher-speed MOS capacitor modulation showing 15 GHz bandwidth in the same 50  $\mu\text{m}$  diameter design [26] and photon-photon resonance [101], [10] are being explored to be efficient alternative solutions to reach 25 Gb/s target. New CMOS driver chips fabricated at 28 nm node were just arrived from the foundry during manuscript preparation. It will provide better matched high-speed drive to QD microring lasers with lower power consumption as well as high-speed voltage modulation to the MOS capacitor.

### ACKNOWLEDGMENT

The authors would like to thank Nanofabrication Facilities at UC-Santa Barbara, and useful discussion with Dr. A. Davis and Dr. N. McDonald at Hewlett Packard Labs.

### REFERENCES

- [1] D. A. B. Miller, "Optical interconnects to electronic chips," *Appl. Opt.*, vol. 49, pp. F59–F70, 2010.
- [2] K. M. Bresnaker, S. Singhal, and R. S. Williams, "Adapting to thrive in a new economy of memory abundance," *Computer*, vol. 48, pp. 44–53, 2015.
- [3] K. Keeton, S. Singhal, and M. Raymond, "The OpenFAM API: A programming model for disaggregated persistent memory," in *Proc. Workshop OpenSHMEM Related Technol.*, 2019, pp. 70–89.

- [4] 2017. [Online]. Available: <https://www.labs.hpe.com/memory-driven-computing>
- [5] 2017. [Online]. Available: <https://news.hpe.com/u-s-dept-of-energy-taps-hewlett-packard-enterprises-machine-research-project-to-design-memory-driven-supercomputer-2/>
- [6] 2018. [Online]. Available: <https://www.labs.hpe.com/next-next/exascale>
- [7] M. A. Taubenblatt, "Optical interconnects for high-performance computing," *J. Lightw. Technol.*, vol. 30, no. 4, pp. 448–457, Feb. 2012.
- [8] R. G. Beausoleil *et al.*, "A nanophotonic interconnect for high-performance many-core computation," in *Proc. 16th IEEE Symp. High Perform. Interconnects*, 2008, pp. 182–189.
- [9] E. Maniloff, S. Gareau, and M. Moyer, "400G and beyond: Coherent evolution to high-capacity inter data center links," in *Proc. Opt. Fiber Commun. Conf., OSA*, 2019, Paper M3H.4.
- [10] S. Yamaoka *et al.*, "239.3-Gbit/s net rate PAM-4 transmission using directly modulated membrane lasers on high-thermal-conductivity SiC," in *Proc. Eur. Conf. Opt. Commun.*, Dublin, Ireland, 2019, Paper PD.2.1.
- [11] P. O. Weigel *et al.*, "Bonded thin film lithium niobate modulator on a silicon photonics platform exceeding 100 GHz 3-dB electrical modulation bandwidth," *Opt. Exp.*, vol. 26, pp. 23728–23739, 2018.
- [12] M. Georgas, J. Leu, B. Moss, C. Sun, and V. Stojanović, "Addressing link-level design tradeoffs for integrated photonic interconnects," in *Proc. IEEE Custom Integr. Circuits Conf.*, 2011, pp. 1–8.
- [13] N. Binkert *et al.*, "Optical high radix switch design," *IEEE Micro*, vol. 32, no. 3, pp. 100–109, May/June 2012.
- [14] C. Doerr and L. Chen, "Silicon photonics in optical coherent systems," *Proc. IEEE*, vol. 106, no. 12, pp. 2291–2301, Dec. 2018.
- [15] A. W. Fang, H. Park, O. Cohen, R. Jones, M. J. Paniccia, and J. E. Bowers, "Electrically pumped hybrid AlGaInAs-silicon evanescent laser," *Opt. Exp.*, vol. 14, pp. 9203–9210, 2006.
- [16] G. Roelkens *et al.*, "Integration of InP/InGaAsP photodetectors onto silicon-on-insulator waveguide circuits," *Opt. Exp.*, vol. 13, pp. 10102–10108, 2005.
- [17] G. Roelkens, D. Van Thourhout, R. Baets, R. Notzel, and M. Smit, "Laser emission and photodetection in an InP/InGaAsP layer integrated on and coupled to a silicon-on-insulator waveguide circuit," *Opt. Exp.*, vol. 14, pp. 8154–8159, 2006.
- [18] H. Park *et al.*, "A hybrid AlGaInAs-silicon evanescent preamplifier and photodetector," *Opt. Exp.*, vol. 15, pp. 13539–13546, 2007.
- [19] T. Komljenovic *et al.*, "Heterogeneous silicon photonic integrated circuits," *J. Lightw. Technol.*, vol. 34, no. 1, pp. 20–35, Jan. 2016.
- [20] S. Matsuo, "Chapter two—Heterogeneously integrated III–V photonic devices on Si," in *Semiconductors and Semimetals*, S. Lourduoss, J. E. Bowers, and C. Jagadish, Eds., Amsterdam, The Netherlands: Elsevier, 2019, pp. 43–89.
- [21] R. Jones *et al.*, "Heterogeneously integrated InP/silicon photonics: Fabricating fully functional transceivers," *IEEE Nanotechnol. Mag.*, vol. 13, no. 2, pp. 17–26, Apr. 2019.
- [22] D. Liang, X. Huang, G. Kurczveil, M. Fiorentino, and R. G. Beausoleil, "Integrated finely tunable microring laser on silicon," *Nature Photon.*, vol. 10, pp. 719–722, 2016.
- [23] T. Hiraki *et al.*, "Heterogeneously integrated III–V/Si MOS capacitor Mach–Zehnder modulator," *Nature Photon.*, vol. 11, pp. 482–485, 2017.
- [24] J.-H. Han, F. Boeuf, J. Fujikata, S. Takahashi, S. Takagi, and M. Takenaka, "Efficient low-loss InGaAsP/Si hybrid MOS optical modulator," *Nature Photon.*, vol. 11, pp. 486–490, 2017.
- [25] A. Roshan-Zamir *et al.*, "A 14 Gb/s directly modulated hybrid microring laser transmitter," in *Proc. Opt. Fiber Commun. Conf.*, San Diego, CA, USA, 2018, Paper M11.7.
- [26] D. Liang *et al.*, "A fully-integrated multi- $\lambda$  hybrid DML transmitter," in *Proc. Opt. Fiber Commun. Conf.*, San Diego, CA, USA, 2019, Paper Th3B.5.
- [27] C. Zhang, D. Liang, G. Kurczveil, A. Descos, and R. G. Beausoleil, "Hybrid quantum-dot microring laser on silicon," *Optica*, vol. 6, pp. 1145–1151, 2019.
- [28] Y.-H. Fan *et al.*, "A directly modulated quantum dot microring laser transmitter with integrated CMOS driver," in *Proc. Opt. Fiber Commun. Conf.*, San Diego, CA, USA, 2019, Paper W3E.5.
- [29] [Online]. Available: <https://www.nextplatform.com/2019/09/09/inside-hpes-gen-z-switch-fabric/>
- [30] C.-H. Chen *et al.*, "A comb laser-driven DWDM silicon photonic transmitter based on microring modulators," *Opt. Exp.*, vol. 23, pp. 21541–21548, 2015.
- [31] Y. Kang *et al.*, "Epitaxially-grown Ge/Si avalanche photodiodes for 1.3  $\mu$ m light detection," *Opt. Exp.*, vol. 16, pp. 9365–9371, 2008.
- [32] Z. Huang *et al.*, "25 Gbps low-voltage waveguide Si-Ge avalanche photodiode," *Optica*, vol. 3, pp. 793–798, 2016.
- [33] J. Van Campenhout *et al.*, "A compact SOI-integrated multiwavelength laser source based on cascaded InP microdisks," *IEEE Photon. Technol. Lett.*, vol. 20, no. 16, pp. 1345–1347, Aug. 2008.
- [34] D. Liang *et al.*, "Electrically-pumped compact hybrid silicon microring lasers for optical interconnects," *Opt. Exp.*, vol. 17, pp. 20355–20364, 2009.
- [35] M. Fujita, A. Sakai, and T. Baba, "Ultrasmall and ultralow threshold GaInAsP-InP microdisk injection lasers: Design, fabrication, lasing characteristics, and spontaneous emission factor," *IEEE J. Sel. Topics Quantum Electron.*, vol. 5, no. 3, pp. 673–681, May/June 1999.
- [36] N. V. Kryzhanovskaya, M. V. Maximov, and A. E. Zhukov, "Whispering-gallery mode microcavity quantum-dot lasers," *Quantum Electron.*, vol. 44, pp. 189–200, 2014.
- [37] G. Mezosi, M. J. Strain, S. Furst, Z. Wang, S. Yu, and M. Sorel, "Unidirectional bistability in AlGaInAs microring and microdisk semiconductor lasers," *IEEE Photon. Technol. Lett.*, vol. 21, no. 2, pp. 88–90, Jan. 2009.
- [38] G. Yuan and S. Yu, "Analysis of dynamic switching behavior of bistable semiconductor ring lasers triggered by resonant optical pulse injection," *IEEE J. Sel. Topics Quantum Electron.*, vol. 13, no. 5, pp. 1227–1234, Sep./Oct. 2007.
- [39] M. Sorel, P. J. R. Laybourn, G. Giuliani, and S. Donati, "Unidirectional bistability in semiconductor waveguide ring lasers," *Appl. Phys. Lett.*, vol. 80, pp. 3051–3053, 2002.
- [40] L. Liu *et al.*, "An ultra-small, low-power, all-optical flip-flop memory on a silicon chip," *Nature Photon.*, vol. 4, pp. 182–187, 2010.
- [41] M. T. Hill *et al.*, "A fast low-power optical memory based on coupled micro-ring lasers," *Nature*, vol. 432, pp. 206–209, 2004.
- [42] J. V. Campenhout *et al.*, "Thermal characterization of electrically injected thin-film InGaAsP microdisk lasers on Si," *J. Lightw. Technol.*, vol. 25, no. 6, pp. 1543–1548, Jun. 2007.
- [43] M. N. Sysak *et al.*, "Hybrid silicon evanescent laser technology: A thermal perspective," *IEEE J. Sel. Topics Quantum Electron.*, vol. 17, no. 6, pp. 1490–1498, Apr. 2011.
- [44] D. Liang and J. E. Bowers, "Recent progress in lasers on silicon," *Nature Photon.*, vol. 4, pp. 511–517, 2010.
- [45] A. Lee, H. Liu, and A. Seeds, "Semiconductor III-V lasers monolithically grown on Si substrates," *Semicond. Sci. Technol.*, vol. 28, 2012, Art. no. 015027.
- [46] J. C. Norman, D. Jung, Y. Wan, and J. E. Bowers, "Perspective: The future of quantum dot photonic integrated circuits," *APL Photon.*, vol. 3, 2018, Art. no. 030901.
- [47] Y. Wan, J. Norman, and J. E. Bowers, "Quantum dot microcavity lasers on silicon substrates," in *Future Directions in Silicon Photonics*, S. Lourduoss, J. E. Bowers, and C. Jagadish, Eds., New York, NY, USA: Academic, 2019, pp. 305–354.
- [48] S. Sui, M. Tang, Y. Yang, J. Xiao, Y. Du, and Y. Huang, "Sixteen-wavelength hybrid AlGaInAs/Si microdisk laser array," *IEEE J. Quantum Electron.*, vol. 51, no. 4, Apr. 2015, Art. no. 2600108.
- [49] G. Roelkens *et al.*, "III–V/silicon photonics for on-chip and intra-chip optical interconnects," *Laser Photon. Rev.*, vol. 4, pp. 751–779, 2010.
- [50] D. Jung *et al.*, "Impact of threading dislocation density on the lifetime of InAs quantum dot lasers on Si," *Appl. Phys. Lett.*, vol. 112, 2018, Art. no. 153507.
- [51] Y. Wan *et al.*, "1.3  $\mu$ m submilliwatt threshold quantum dot micro-lasers on Si," *Optica*, vol. 4, pp. 940–944, 2017.
- [52] M. O'teen *et al.*, "Chapter 29 - systems and technology for Production-Scale molecular beam epitaxy," in *Molecular Beam Epitaxy*, 2nd ed., Amsterdam, The Netherlands: Elsevier, 2018, pp. 649–675.
- [53] D. Dai, D. Liang, and J. E. Bowers, "Enhancement of the evanescent coupling between deeply-etched III-V-Si hybrid microring laser and its small Si bus waveguide by using a bending coupler," in *Proc. Asia Commun. Photon. Conf. Exhib.*, 2009, Paper TuP5.
- [54] C. Zhang, D. Liang, G. Kurczveil, J. E. Bowers, and R. G. Beausoleil, "Thermal management of hybrid silicon ring lasers for high temperature operation," *IEEE J. Sel. Topics Quantum Electron.*, vol. 21, no. 6, pp. 385–391, Nov./Dec. 2015.
- [55] D. Liang, G. Kurczveil, M. Fiorentino, S. Srinivasan, J. E. Bowers, and R. G. Beausoleil, "A tunable hybrid III–V-on-Si MOS microring resonator with negligible tuning power consumption," in *Proc. Opt. Fiber Commun. Conf. Exhib.*, Anaheim, CA, USA, 2016, Paper Th1K.4.
- [56] B. R. Bennett, R. A. Soref, and J. A. D. Alamo, "Carrier-induced change in refractive index of InP, GaAs and InGaAsP," *J. Quantum Electron.*, vol. 26, pp. 113–122, 1990.

- [57] R. Soref and B. Bennett, "Electrooptical effects in silicon," *IEEE J. Quantum Electron.*, vol. QE-23, no. 1, pp. 123–129, Jan. 1987.
- [58] G. Ortner *et al.*, "External cavity InAs/InP quantum dot laser with a tuning range of 166nm," *Appl. Phys. Lett.*, vol. 88, 2006, Art. no. 121119.
- [59] X. Huang *et al.*, "Heterogeneous MOS microring resonators," in *Proc. Photon. Conf.*, Orlando, FL, USA, 2017, pp. 121–122.
- [60] C. Chen *et al.*, "Hybrid integrated DWDM silicon photonic transceiver with self-adaptive CMOS circuits," in *Proc. Opt. Interconnects Conf.*, Santa Fe, NM, USA, 2013, pp. 122–123.
- [61] G. Kurczveil, C. Zhang, A. Descos, D. Liang, M. Fiorentino, and R. G. Beausoleil, "On-chip hybrid silicon quantum dot comb laser with 14 error-free channels," in *Proc. IEEE Int. Semicond. Laser Conf.*, Santa Fe, NM, USA, 2018, pp. 1–2.
- [62] G. Kurczveil, A. Seyedi, D. Liang, M. Fiorentino, and R. G. Beausoleil, "Error-free operation in a hybrid-silicon quantum dot comb laser," *Photon. Technol. Lett.*, vol. 30, pp. 71–74, 2018.
- [63] G. Kurczveil, D. Liang, M. Fiorentino, and R. G. Beausoleil, "Robust hybrid quantum dot laser for integrated silicon photonics," *Opt. Exp.*, vol. 24, pp. 16167–16174, 2016.
- [64] C. Zhang, D. Liang, G. Kurczveil, A. Descos, and R. G. Beausoleil, "Error-free 12.5 Gb/s direct modulation of low-threshold hybrid QD microring laser," in *Proc. Eur. Conf. Opt. Commun.*, Rome, Italy, 2018, pp. 1–3.
- [65] C. Zhang, D. Liang, G. Kurczveil, and R. G. Beausoleil, "High speed QDs microring lasers on silicon," in *Proc. Eur. Conf. Integr. Opt.*, Valencia, Spain, 2018, Paper Th.2.A.2.
- [66] B. Tossoun, G. Kurczveil, C. Zhang, D. Liang, and R. G. Beausoleil, "High-speed 1310 nm hybrid silicon quantum dot photodiodes with Ultra-low dark current," in *Proc. Device Res. Conf.*, Santa Barbara, CA, USA, 2018, pp. 1–2.
- [67] B. Tossoun *et al.*, "InAs quantum dot waveguide photodiodes heterogeneously integrated on silicon," *Optica*, vol. 6, pp. 1277–1281, 2019.
- [68] G. Park, O. B. Shchekin, D. L. Huffaker, and D. G. Deppe, "Low-threshold oxide-confined 1.3- $\mu\text{m}$  quantum-dot laser," *Photon. Technol. Lett.*, vol. 12, pp. 230–232, 2000.
- [69] T. Kageyama *et al.*, "Extremely high temperature (220oC) continuous-wave operation of 1300-nm-range quantum-dot lasers," in *Proc. Conf. Lasers Electro-Opt. Eur.*, 12th Eur. Quantum Electron. Conf., 2011, Paper PDA\_1.
- [70] M. Sugawara and M. Usami, "Quantum dot devices: Handling the heat," *Nature Photon.*, vol. 3, pp. 30–31, 2009.
- [71] A. Capua *et al.*, "Direct correlation between a highly damped modulation response and ultra low relative intensity noise in an InAs/GaAs quantum dot laser," *Opt. Exp.*, vol. 15, pp. 5388–5393, 2007.
- [72] H. Huang *et al.*, "Analysis of the optical feedback dynamics in InAs/GaAs quantum dot lasers directly grown on silicon," *J. Opt. Soc. Amer. B*, vol. 35, pp. 2780–2787, 2018.
- [73] S. A. Moore, L. O. Faolain, M. A. Cataluna, M. B. Flynn, M. V. Kotlyar, and T. F. Krauss, "Reduced surface sidewall recombination and diffusion in quantum-dot lasers," *Photon. Technol. Lett.*, vol. 18, pp. 1861–1863, 2006.
- [74] J. Van Campenhout *et al.*, "Electrically pumped InP-based microdisk lasers integrated with a nanophotonic silicon-on-insulator waveguide circuit," *Opt. Exp.*, vol. 15, pp. 6744–6749, 2007.
- [75] T. Spuesens, L. Liu, T. d. Vries, P. R. Romeo, P. Regreny, and D. V. Thourhout, "Improved design of an InP-based microdisk laser heterogeneously integrated with SOI," in *Proc. 6th IEEE Int. Conf. Group IV Photon.*, 2009, pp. 202–204.
- [76] I. R. Sellers *et al.*, "1.3  $\mu\text{m}$  InAs/GaAs multilayer quantum-dot laser with extremely low room-temperature threshold current density," *Electron. Lett.*, vol. 40, pp. 1412–1413, 2004.
- [77] K. Tanabe and Y. Arakawa, "1.3  $\mu\text{m}$  InAs/GaAs quantum dot lasers on SOI waveguide structures," in *Proc. Conf. Lasers Electro-Opt., OSA*, 2014, Paper STh1G.6.
- [78] R. R. Alexander *et al.*, "Systematic study of the effects of modulation P-doping on 1.3  $\mu\text{m}$  InAs/GaAs dot-in-well lasers," in *Proc. IEEE 19th Int. Conf. Indium Phosphide Related Mater.*, 2007, pp. 517–520.
- [79] K. Li *et al.*, "O-band InAs/GaAs quantum dot laser monolithically integrated on exact (011) Si substrate," *J. Crystal Growth*, vol. 511, pp. 56–60, 2019.
- [80] J. Kwoen, B. Jang, K. Watanabe, and Y. Arakawa, "High-temperature continuous-wave operation of directly grown InAs/GaAs quantum dot lasers on on-axis Si (001)," *Opt. Exp.*, vol. 27, pp. 2681–2688, 2019.
- [81] D. Liang *et al.*, "Teardrop reflector-assisted unidirectional hybrid-silicon microring lasers," *IEEE Photon. Technol. Lett.*, vol. 24, no. 22, pp. 1988–1990, Nov. 2012.
- [82] A. Arbabi, S. M. Kamali, E. Arbabi, B. G. Griffin, and L. L. Goddard, "Grating integrated single mode microring laser," *Opt. Exp.*, vol. 23, pp. 5335–5347, 2015.
- [83] L. V. Asryan and R. A. Suris, "Inhomogeneous line broadening and the threshold current density of a semiconductor quantum dot laser," *Semicond. Sci. Technol.*, vol. 11, pp. 554–567, 1996.
- [84] M. N. Sysak *et al.*, "Experimental and theoretical thermal analysis of a hybrid silicon evanescent laser," *Opt. Exp.*, vol. 15, pp. 15041–15046, 2007.
- [85] D. Liang *et al.*, "Optimization of hybrid silicon microring lasers," *IEEE Photon. J.*, vol. 3, no. 3, pp. 580–587, Jun. 2011.
- [86] M. Raj, M. Monge, and A. Emami, "A modelling and nonlinear equalization technique for a 20 Gb/s 0.77 pJ/b VCSEL transmitter in 32 nm SOI CMOS," *IEEE J. Solid-State Circuits*, vol. 51, no. 8, pp. 1734–1743, Aug. 2016.
- [87] A. E. Zhukov, M. V. Maksimov, and A. R. Kovsh, "Device characteristics of long-wavelength lasers based on self-organized quantum dots," *Semiconductors*, vol. 46, pp. 1225–1250, 2012.
- [88] Y.-H. Jhang *et al.*, "Direct modulation of 1.3  $\mu\text{m}$  quantum dot lasers on silicon at 60 °C," *Opt. Exp.*, vol. 24, pp. 18428–18435, 2016.
- [89] D. Inoue *et al.*, "Directly modulated 1.3  $\mu\text{m}$  quantum dot lasers epitaxially grown on silicon," *Opt. Exp.*, vol. 26, pp. 7022–7033, 2018.
- [90] Y. Wan *et al.*, "Directly modulated quantum dot lasers on silicon with a milliampere threshold and high temperature stability," *Photon. Res.*, vol. 6, pp. 776–781, 2018.
- [91] K. Nakahara *et al.*, "Direct modulation at 56 and 50 Gb/s of 1.3-  $\mu\text{m}$  InGaAlAs ridge-shaped-BH DFB lasers," *IEEE Photon. Technol. Lett.*, vol. 27, no. 5, pp. 534–536, Mar. 2015.
- [92] S. Matsuo, T. Fujii, K. Hasebe, K. Takeda, T. Sato, and T. Kakitsuka, "Directly modulated DFB laser on SiO<sub>2</sub>/Si substrate for datacenter networks," *J. Lightw. Technol.*, vol. 33, no. 6, pp. 1217–1222, Mar. 2015.
- [93] S. Matsuo and T. Kakitsuka, "Low-operating-energy directly modulated lasers for short-distance optical interconnects," *Advances Opt. Photon.*, vol. 10, pp. 567–643, 2018.
- [94] S. Sui, Y. Huang, M. Tang, Y. Yang, J. Xiao, and Y. Du, "Hybrid deformed-riding AlGaInAs/Si microlasers with stable unidirectional emission," *IEEE J. Sel. Topics Quantum Electron.*, vol. 23, no. 6, Nov./Dec. 2017, Art. no. 1500308.
- [95] P. Mechet *et al.*, "Unidirectional III-V microdisk lasers heterogeneously integrated on SOI," *Opt. Exp.*, vol. 21, pp. 19339–19352, 2013.
- [96] M. Kneissl, M. Teepe, N. Miyashita, N. M. Johnson, G. D. Chern, and R. K. Chang, "Current-injection spiral-shaped microcavity disk laser diodes with unidirectional emission," *Appl. Phys. Lett.*, vol. 84, pp. 2485–2487, 2004.
- [97] J. P. Hohimer, G. A. Vawter, and D. C. Craft, "Unidirectional operation in a semiconductor ring diode laser," *Appl. Phys. Lett.*, vol. 62, pp. 1185–1187, 1993.
- [98] J. P. Hohimer and G. A. Vawter, "Unidirectional semiconductor ring lasers with racetrack cavities," *Appl. Phys. Lett.*, vol. 63, pp. 2457–2459, 1993.
- [99] H. Hodaie, M.-A. Miri, M. Heinrich, D. N. Christodoulides, and M. Khajavikhan, "Parity-time-symmetric microring lasers," *Science*, vol. 346, pp. 975–978, 2014.
- [100] B. Dong *et al.*, "Optical injection in a hybrid-silicon quantum dot comb laser," *Opt. Lett.*, vol. 44, no. 23, pp. 5755–5758, 2019.
- [101] D. Liang *et al.*, "Optical injection-locked high-speed heterogeneous quantum-dot microring lasers," in *Proc. Eur. Conf. Opt. Commun.*, Dublin, Ireland, 2019, Paper Th.2.D.

**Di Liang** (S'02–M'07–SM'14) received the B.S. degree from Zhejiang University, Hangzhou, China, in 2002 and the M.S. and Ph.D. degrees from the University of Notre Dame, Notre Dame, IN, USA, in 2004 and 2006 respectively. He is currently a Senior Research Scientist with Hewlett Packard Labs in Hewlett Packard Enterprise, Palo Alto, CA, USA. He is leading advanced III-V and silicon photonics research in HPE and is currently a Principal Investigator for multiple US government funded R&D programs. Prior to joining HP Labs, he was a Core Researcher in the early stage R&D of the hybrid III/V-on-silicon photonic platform which has been commercialized by Intel and Juniper Networks (Aurion) recently. His research interests include diode lasers, integrated photonics, heterogeneous and monolithic material integration, and nanofabrication technology for communications, computing, and sensing applications. He has authored or coauthored around 200 journal and conference papers, five book chapters, and was granted by 29 patents with another more than 55 pending.

**Ashkan Roshan-Zamir** (S'14–M'19) received the B.Sc. and M.Sc. degrees in electrical engineering from the University of Tehran, Tehran, Iran, in 2010 and 2013, respectively, and the Ph.D. degree in electrical engineering from Texas A&M University, College Station, TX, USA, in 2018.

He was with Samsung Semiconductor Inc., San Jose, CA, USA, as a Design Intern in 2015, where he was involved in the design of clock and data recovery systems. He was with Texas Instruments Incorporated, Duluth, GA, USA as a Design Intern, in 2017, where he was involved in the design of integrated circuits for high-speed wireline communication. In 2018, he joined Texas Instruments, Santa Clara, CA, USA, as a Design Engineer, where he is involved in designing integrated mixed-signal circuits and circuits for wireline and optical communication. His current research interests include analog and mixed-signal integrated circuits, high speed circuits for electrical and optical communication, and clock and data recovery circuits.

**Yang-Hang Fan** received the B.S. degree in engineering and system science and the M.S. degree from the Institute of Electronics Engineering, National Tsing Hua University, Hsinchu, Taiwan, in 2007 and 2009, respectively. He is currently working toward the Ph.D. degree in electrical engineering with Texas A&M University, College Station, TX, USA.

From 2011 to 2015, he was with Faraday Technology, Hsinchu, Taiwan, where he worked on the design of mixed-signal integrated circuits for high-speed wireline communication. He was a Design Intern with Hewlett Packard Enterprise, Palo Alto, CA, USA, where he was involved in the design of integrated circuits for high-speed optical communication. Since 2016, he has been a Research Assistant with the Analog and Mixed Signal Center, Texas A&M University. His current research interests include mixed-signal integrated circuits and high-speed circuits for electrical and optical links.

**Chong Zhang** received the B.S. degree in electrical science and technology from the Harbin Institute of Technology, Harbin, China, in 2007, the M.S. degree in optical engineering from Zhejiang University, Hangzhou, China, in 2010, and the Ph.D. degree in electrical and computer engineering from the University of California, Santa Barbara, CA, USA, in 2017. He worked with Hewlett Packard Labs between 2016 and 2018 and is currently with Nexus Photonics, Inc. He has authored or coauthored more than 80 journal and conference papers in the field of semiconductor material epitaxy, heterogeneous integration, and photonic circuits in the applications of optical interconnects.

**Binhao Wang** (M'16) received the B.S. degree in electrical engineering and the M.S. degree in optical engineering from Zhejiang University, Hangzhou, China, in 2008 and 2011, respectively, and the Ph.D. degree in electrical engineering from Texas A&M University, College Station, TX, USA, in 2016. He is a Research Scientist with the Systems Architecture Laboratory, Hewlett Packard Laboratories, Hewlett Packard Enterprise, Palo Alto, CA, USA. He has authored or coauthored more than 40 peer-reviewed journal and conference papers. His research interests include VCSEL photonics and silicon photonics.

**Antoine Descos** received the graduate degree in microtechnology from the French Engineer School, Ecole Centrale de Lyon, Écully, France, in 2010, the master's degree in microtechnology from University Claude Bernard Lyon 1, Villeurbanne, France, in 2010, and the Ph.D. degree in physics from Ecole Centrale de Lyon, Écully, France, in 2014, working with the CEA-LETI in Grenoble. He is currently a Research Engineer in Large Scale Integrated Photonics with the Systems Research Laboratory, Hewlett Packard Labs, Palo Alto, CA, USA. His research is mainly focused on the hybrid III-V on silicon lasers technology. He has designed, fabricated, and characterized different laser kind mainly for telecommunication purpose. He participated in 40 papers and conference proceedings.

**Wenqing Shen** received the B.S. degree from the Huazhong University of Science and Technology, Wuhan, China, in 2009 and the master's degree in mechanical engineering from Rutgers University, New Brunswick, NJ, USA, in 2018. He is currently working toward the Ph.D. degree in thermal property study of semiconductor devices with Georgia Institute of Technology, Atlanta, GA, USA, where he works in Dr. Satish Kumar's group. His research interests include nanoscale and microscale simulation, thermal property measurement and thermal management of semiconductors, and electronic devices.

**Kunzhi Yu** (S'14) received the B.S. degree from Shanghai Jiao Tong University, Shanghai, China, in 2008, the M.E. degree from Tsinghua University, Beijing, China, in 2013, and the Ph.D. degree in electrical engineering from Texas A&M University, College Station, TX, USA, in 2018. From 2015 to 2017, he was a Research Intern and a Visiting Researcher with Hewlett Packard Labs, Palo Alto, CA, USA. During the summer of 2015, he was a Design Intern with Texas Instruments Kilby Labs, Dallas, TX, USA. Since 2015, he has been with a startup that he co-founded in Santa Clara, CA, USA. His research interests include high-speed transceiver circuits design for optical and photonic links, RF photonics systems, and LIDAR/3D image sensing systems.

**Cheng Li** received the B.S. degree in electrical engineering from Southeast University, Nanjing, China, in 2001, the M.S. degree in computer engineering from the Illinois Institute of Technology, Chicago, IL, USA, in 2009, and the Ph.D. degree in electrical engineering from Texas A&M University, College Station, TX, USA, in 2013. From 2001 to 2007, he was with Alcatel-Lucent, Shanghai, China, where he worked with Central R&D on the design of broadband DSLAM 7300 access systems. From 2013 to 2017, he was a Senior Research Scientist with Hewlett Packard Laboratories, Palo Alto, CA, USA, where his research interests include the design of high-speed transceiver circuits for optical/photonic links, photonic interconnects for high-performance computing, and LIDAR/Image sensing systems. In 2017, he founded visionICs, a pioneer working on the 3-D vision sensor for robotics sensing. He has authored or coauthored more than 50 peer-reviewed journal and conference papers. He owns more than 10 pending U.S. patents. He has been a Member of the Technical Program Committee of the IEEE Compound Semiconductor IC Symposium, the IEEE 58th Midwest Symposium on Circuits and Systems, and a KTMA Member of the American Institute for Manufacturing Integrated Photonics (AIM).

**Gaofeng Fan** received the B.S. degree in communication engineering from the Beijing University of Posts and Telecommunications, Beijing, China, in 2010 and the M.Eng. degrees from Nanyang Technological University, Singapore and Texas A&M University, College Station, TX, USA, in 2013 and 2017, respectively. He is currently with Microchip, Austin, TX, USA, where he designs analog high-speed ethernet interface for automobile applications. Prior to this, he worked at Xilinx Singapore as a Signal Integrity Engineer.

**Geza Kurczveil** (M'12) received the Ph.D. degree in electrical and computer engineering from the University of California, Santa Barbara, CA, USA, in 2012, working on optical buffers. He is currently a Research Scientist with Hewlett Packard Labs, Palo Alto, CA, USA. His current research interests include silicon photonic integrated circuits and nano-photonics. He has authored or coauthored more than 50 journal and conference papers.

**Yingtao Hu** received the B.S. degree in material science from Central South University, Changsha, China, in 2007 and the Ph.D. degree in physical electronics from the Institute of Semiconductors, Chinese Academy of Sciences, Beijing, China, in 2012. From 2012 to 2015, he was a Postdoc with IMEC and University of Ghent, Belgium, where he has been working on graphene modulators on silicon. He is currently a Research Scientist with Hewlett Packard Labs, Palo Alto, CA, USA. His research interests focus on hybrid III-V-on-Si lasers and III-V to Si integration.

**Zhihong Huang** (SM'18) received the B.S. degree from Peking University, Beijing, China, and the M.S. and Ph.D. degrees in electrical engineering from the University of Texas at Austin, Austin, TX, USA. She is currently a Research Scientist with Hewlett Packard Labs, Palo Alto, CA, USA, leading the development of low power optical transceivers for optical interconnects. Her research interests include avalanche photodiodes, single photon counting, optical sensors, nano-photonics, silicon photonics, and quantum information processing. She has authored or coauthored more than 80 journal and conference papers and was granted more than 20 US/international patents with another dozen pending.

**Marco Fiorentino** received the Ph.D. degree in physics from the University of Napoli, Naples, Italy, in 2000, working on quantum optics. He is a Distinguished Technologist with the Systems Architecture Lab, Hewlett Packard Laboratories, Palo Alto, CA, USA. He is currently working on productizing silicon photonics technologies for computer interconnects. Before joining Hewlett Packard in 2005, he worked with Northwestern University, the University of Rome, and MIT.

**Satish Kumar** received the B.Tech. degree in mechanical engineering from the Indian Institute of Technology, Guwahati, India, in 2001 and the M.S. degree in electrical and computer engineering, in 2005 and the Ph.D. degree in mechanical engineering from Purdue University, West Lafayette, IN, USA, in 2007. He is currently an Associate Professor with George W. Woodruff School of Mechanical Engineering, Georgia Tech, Atlanta, GA, USA. Prior to joining Georgia Tech in 2009, he worked at IBM Corporation, where he was responsible for the thermal management of electronic devices. His research interests include electro-thermal transport study in nano-structures and electronic devices, wide band-gap devices, and flexible-electronics. He has authored or coauthored more than 100 journal or conference publications. He was the recipient of the 2005 Purdue Research Foundation Fellowship, the 1969 Teaching Fellow from the Center for the Enhancement of Teaching and Learning Center at Georgia Tech, the 2012 Summer Faculty Fellow from Air Force Research Lab, the 2014 Sigma Xi Young Faculty Award, the 2014 DARPA Young Faculty Award, the 2017 Woodruff Faculty Fellow Award, and the 2019 ASME Fellow Award.

**Samuel M. Palermo** (S'98–M'07–SM'17) received the B.S. and M.S. degrees in electrical engineering from Texas A&M University, College Station, TX, USA, in 1997 and 1999, respectively, and the Ph.D. degree in electrical engineering from Stanford University, Stanford, CA, USA, in 2007.

From 1999 to 2000, he was with Texas Instruments, Dallas, TX, USA, where he worked on the design of mixed-signal integrated circuits for high-speed serial data communication. From 2006 to 2008, he was with Intel Corporation, Hillsboro, OR, USA, where he worked on high-speed optical and electrical I/O architectures. In 2009, he joined the Electrical and Computer Engineering Department, Texas A&M University, College Station, TX, USA, where he is currently an Associate Professor. His research interests include high-speed electrical and optical interconnect architectures, RF photonics, high performance clocking circuits, and integrated sensor systems.

He was the recipient of a 2013 NSF-CAREER Award. He is a Member of Eta Kappa Nu. He is currently an Associate Editor for the IEEE SOLID-STATE CIRCUITS LETTERS and has previously served as an Associate Editor for the IEEE TRANSACTIONS ON CIRCUITS AND SYSTEMS-II. He has also previously served as a Distinguished Lecturer for the IEEE Solid-State Circuits Society and on the IEEE CASS Board of Governors. He was a coauthor of the Jack Raper Award for Outstanding Technology-Directions Paper at the 2009 International Solid-State Circuits Conference, the Best Student Paper Award at the 2014 Midwest Symposium on Circuits and Systems, and the Best Student Paper Award at the 2016 Dallas Circuits and Systems Conference. He received the Texas A&M University Department of Electrical and Computer Engineering Outstanding Professor Award in 2014 and the Engineering Faculty Fellow Award in 2015.

**Raymond G. Beausoleil** (F'17) received the B.S. degree from Caltech, Pasadena, CA, USA, in 1980 and the Ph.D. degree from Stanford University, Stanford, CA, USA, in 1986, both in physics. He is currently a Senior Fellow and the Senior Vice President with Hewlett Packard Enterprise (HPE), San Jose, CA, USA, where he leads the Large-Scale Integrated Photonics Research Group with Hewlett Packard Labs. Prior to HPE, his research was focused on high-power all-solid-state laser and nonlinear optical systems, as well as numerical algorithms for computer firmware (leading to the navigation algorithms for the optical mouse). At Hewlett Packard Labs, he performs basic and applied research in microscale and nanoscale classical and quantum optics for information processing technologies. He is an Adjunct Professor of Applied Physics with Stanford University, a Fellow of the American Physical Society and the Optical Society of America, and the recipient of the 2016 APS Distinguished Lectureship on the Applications of Physics. He has contributed to more than 400 papers and conference proceedings (including many invited papers and plenary/keynote addresses) and five book chapters. He has more than 150 patents issued and more than four dozen pending.